Commun Nonlinear Sci Numer Simulat 70 (2019) 48–73

Contents lists available at ScienceDirect

Commun Nonlinear Sci Numer Simulat

journal homepage: www.elsevier.com/locate/cnsns

Research paper

Gluing and grazing bifurcations in periodically forced 2-dimensional integrate-and-fire models

Albert Granados [a,*], Gemma Huguet [b]

[a] Department of Applied Mathematics and Computer Science, Technical University of Denmark, Building 303B, 2800 Kgns., Lyngby, Denmark

[b] Department de Matemàtiques, Universitat Politècnica de Catalunya, Av. Diagonal 647, 08028, Barcelona, Spain

ARTICLE INFO

Article history:
Received 13 December 2017
Revised 27 July 2018
Accepted 6 September 2018
Available online 17 October 2018

Keywords:
Integrate-and-fire
Hybrid systems
Piecewise smooth 2d maps
Quasi-contractions

ABSTRACT

In this work we consider a general class of 2-dimensional hybrid systems. Assuming that the system possesses an attracting equilibrium point, we show that, when periodically driven with a square-wave pulse, the system possesses a periodic orbit which may undergo smooth and nonsmooth grazing bifurcations. We perform a semi-rigorous study of the existence of periodic orbits for a particular model consisting of a leaky integrate-and-fire model with a dynamic threshold. We use the stroboscopic map, which in this context is a 2-dimensional piecewise-smooth discontinuous map. For some parameter values we are able to show that the map is a quasi-contraction possessing a (locally) unique max-imin periodic orbit. We complement our analysis using advanced numerical techniques to provide a complete portrait of the dynamics as parameters are varied. We find that for some regions of the parameter space the model undergoes a cascade of gluing bifurcations, while for others the model shows multistability between orbits of different periods.

1. Introduction

Integrate-and-fire systems are hybrid systems that combine continuous dynamics with discrete resets that occur whenever the variables of the system satisfy a given condition (that defines a threshold). Such systems are widely used in neuroscience to model the dynamics of neuron's membrane potential, as the continuous dynamics models subthreshold behaviour (corresponding to the input integration) and resets represent neuron spikes (characteristic rapid changes in membrane potential). They can be seen as simplified versions of slow-fast systems, as the resets replace large amplitude oscillations that occur at a much faster time-scale.

Examples of such systems range from simple one-dimensional models as the leaky integrate-and-fire [1], which models simple repetitive spiking, to nonlinear 2-dimensional ones exhibiting more complicated behaviour, such as the Izhikevich quadratic model [2], or the adaptive exponential model [3]. Of special interest for this paper are 2-dimensional models consisting of an integrate-and-fire model with a dynamic threshold – the threshold is treated as a variable with nonlinear dynamics. These type of systems have been used to model spike threshold variability observed in different areas of the nervous system [4], in particular for phasic neurons (those that do not respond repetitively to steady or slowly varying inputs) in the auditory brainstem [5–7].

* Corresponding author.
E-mail addresses: albert.granados.corsellas@upc.edu (A. Granados), gemma.huguet@upc.edu (G. Huguet).

https://doi.org/10.1016/j.cnsns.2018.09.006
1007-5704/

A general framework to study the dynamics of hybrid systems becomes difficult to obtain, even when the input currents are assumed to be constant (the system remains autonomous), mainly because they are discontinuous due to the reset condition. One of the most common strategies in the nonsmooth literature (see [8,9]) is to smooth the dynamics by considering the so-called *impact map* (also known in neuroscience as *firing phase map* or *adaptation map*) defined on the threshold where the reset condition is applied [10–13]. However, the impact map does not allow one to study itineraries or trajectories that do not hit the threshold and has some domain restrictions.

In more realistic situations one considers periodic inputs, making the analysis more complicated. Indeed, in the non-autonomous case, even one-dimensional integrate-and-fire systems exhibit very rich dynamics [13–15]. Recent works show how theory for nonsmooth systems can be used to obtain model-independent general results [16–18]. However, these are limited to one-dimensional systems exhibiting simple subthreshold dynamics, as they are based on the theory for circle maps (see [19] for a recent review).

In this work we study 2-dimensional hybrid systems subject to periodic forcing. In particular, we consider an input consisting of a square-wave pulse of period T, which can be seen as a simplified model for a periodically varying synaptic current in neuroscience [20] while is widely used in electronics (PWM), amongst others. Our goal is to provide a description of the dynamics to determine the firing patterns that arise in the forced system. Assuming that the unforced system possesses an attracting equilibrium point, we show that, when periodically driven, the system possesses a T-periodic orbit which may undergo smooth-grazing or nonsmooth-grazing bifurcations as the amplitude of the forcing increases and collides with the threshold. To study these bifurcations, we use the stroboscopic map (or time-T map), which becomes a 2-dimensional piecewise-smooth discontinuous map. Indeed, the map is defined differently depending on the number of times the corresponding trajectory of the time-continuous system hits the threshold, thus showing discontinuities along the so-called *switching manifolds*. An orbit of the time-continuous system undergoing a smooth or a nonsmooth grazing bifurcation with the threshold corresponds to a fixed point of the stroboscopic map undergoing a border collision bifurcation when hitting the switching manifold , which we study in detail.

Beyond the fixed points we study other periodic orbits of the stroboscopic map (nT-periodic orbits of the time-continuous system), as well as their itineraries (sequence of regions in the domain of the stroboscopic map visited by the periodic orbits), and their bifurcations. Notice that in this case, the theory for smooth maps does not apply to describe its dynamical properties. Unfortunately, there are little theoretical results to describe these orbits for the cases of maps of dimension higher than 1, in which case one relies on classical results for circle maps [21]. In this paper we recover a result in this direction by Gambaudo et al. in the 80's [22,23]. The theorem establishes conditions for the existence of periodic orbits for a piecewise continuous map of any dimension and provides properties on the sequence of regions visited. We apply this result to a particular model, a leaky integrate-and-fire model with a dynamic threshold. By means of semi-rigorous numerical arguments we can prove that for certain parameter values the stroboscopic map becomes a quasi-contraction possessing *maximin* (locally) unique periodic orbits. That is, their symbolic itineraries are contained in the Farey tree of symbolic sequences [19]. In parallel, we use advanced numerical techniques to provide a complete portrait of the dynamics as parameters are varied. Numerically, we find that for certain parameters the model undergoes a period-adding bifurcation (an infinite cascade of gluing bifurcations [24], up to our numerical accuracy), while for others the model shows multistability between orbits of different periods. Our study allows us to assess the scope of the existing theoretical results.

The paper is organized as follows. In Section 2 we present the general setting for hybrid 2-dimensional systems. In Section 3 we introduce the stroboscopic map, which is a piecewise-smooth discontinuous 2-dimensional map. In Section 4 we describe the border collision bifurcations of the fixed points, a type of bifurcation that can only occur in piecewise-defined maps and in Section 5 we present existing theoretical results for the existence of periodic orbits of a piecewise continuous map which step onto different regions. In Section 6 we use the previous results in combination with numerical methods to describe the dynamics of a leaky integrate-and-fire model with a dynamic threshold. We modify parameters to illustrate different dynamical regimes exhibited by the model. Finally, the Appendix includes the details of the numerical methods used to perform the computations along the paper.

2. General setting

Let us consider the system

$$\dot{z} = f(z) + vI(t), \quad z \in \mathbb{R}^2 \tag{1}$$

with $v \in \mathbb{R}^2$ (typically it will be chosen $v = (1,0)^T$), $f : \mathbb{R}^2 \to \mathbb{R}^2$ a smooth enough function and $I(t)$ a T-periodic square wave given by

$$I(t) = \begin{cases} A & \text{if } t \in (nT, nT + dT] \\ 0 & \text{if } t \in (nT + dT, (n+1)T]. \end{cases}, \ n \in \mathbb{N} \tag{2}$$

Let us also consider a *threshold* manifold $\mathcal{T}$ in $\mathbb{R}^2$ given by

$$\mathcal{T} = \left\{(x,y) \in \mathbb{R}^2 \,|\, h(x,y) = 0\right\},$$

where $h : \mathbb{R}^2 \to \mathbb{R}$ is a smooth function. We then submit system (1) to the following reset condition: whenever a trajectory reaches the threshold manifold $\mathcal{T}$ at a time $t = t_*$, the variables of the system are updated to a certain value, i.e.

$$h(z(t_*)) = 0 \longrightarrow z(t_*^+) = R(z(t_*)), \tag{3}$$

where R is a reset (smooth) map:

$$R: \quad \mathcal{T} \quad \longrightarrow \quad \mathbb{R}^2. \tag{4}$$

We call

$$\mathcal{R} := R(\mathcal{T})$$

the reset manifold. The reset condition (3) is applied whenever a trajectory collides with the threshold manifold $\mathcal{T}$. Following the terminology in neuroscience, from now on, when this occurs we say that system (1)–(3) exhibits a spike. Although, these spikes introduce discontinuities to the trajectories of system (1), they are all well defined, as one just needs to apply the map R whenever the threshold is reached. This induces a flow,

$$\phi(t; t_0, z_0), \quad \phi(t_0; t_0, z_0) = z_0,$$

which, provided that sliding cannot not occur along the threshold manifold, is well defined. The flow however is discontinuous whenever $\mathcal{T}$ is reached and nonsmooth when the pulse $I(t)$ is enabled or disabled.

We are going to assume that for $A = 0$, sytem (1) has an equilibrium point $z^* \in \mathbb{R}^2$ (see *H.1* below). Then, we can define the subthreshold domain as

$$\mathbb{D} = \left\{ z \in \mathbb{R}^2 \mid h(z) \cdot h(z^*) > 0 \right\}. \tag{5}$$

The subthreshold domain contains all points in one side of $\mathcal{T}$ (the same side that contains the equilibrium point for $A = 0$). In many practical applications we will restrict this domain to points in the region delimited by the manifolds $\mathcal{T}$ and $\mathcal{R}$.

Given $z \in \mathbb{D}$, we will say that its trajectory is subthreshold if $\phi(t; t_0, z) \in \mathbb{D}$ for all $t \geq t_0$. In particular, an invariant set is subthreshold if it is contained in $\mathbb{D}$.

We assume that, for $A = 0$, system (1)

H.1 possesses an attracting equilibrium point $z^* \in \mathbb{R}^2$,
H.2 for any $z \in \mathbb{D}$, trajectories are subthreshold, i.e. they do not exhibit spikes.

Remark 1. Hypothesis H.2 could be removed at the price of increasing the complexity of the mathematical analysis (see Remark 3), but we decided to keep it in order to make the presentation clearer. Moreover, we want to emphasize that it is a realistic assumption. Indeed, in Section 6 we consider an integrate-and-fire model which does satisfy hypothesis H.2.

3. The stroboscopic map

3.1. Definition

Since we consider a T-periodic forcing $I(t)$ (see Eq. (2)), we follow [16] and consider the stroboscopic map $\mathfrak{s} : \mathbb{D} \to \mathbb{D}$ defined as:

$$\mathfrak{s}(z) = \phi(t_0 + T; t_0, z).$$

Note that system (1)–(3) is non-autonomous and, therefore, the stroboscopic map depends on the initial time, t_0. However, as t_0 provides a family of conjugated stroboscopic maps, we can assume $t_0 = 0$ from now on and abusing notation we write $\mathfrak{s}(z) = \phi(T; z) = \phi(T; 0, z)$.

As detailed below, depending on the number of spikes exhibited by a solution $\phi(t; z)$ for $t \in [0, T)$, the stroboscopic map becomes a different combination of smooth maps given by integrating Eq. (1) and applying the reset map (4). Hence, this is a piecewise smooth map. More precisely, let us define the sets (see Fig. 1):

$$S_n = \left\{ z \in \mathbb{D} \mid \phi(t; z) \text{ exhibits } n \text{ spikes for } 0 < t \leq dT \right\}, \ n \geq 0. \tag{6}$$

Then, when restricted to S_n, the map $\mathfrak{s}$ becomes a fixed combination of maps alternating the integration of system (1) and the application of the reset map R. Hence, $\mathfrak{s}$ restricted to S_n is as smooth as the map R and the flow of the vector field f, as the sequence of impacts is fixed in S_n.

Remark 2. Notice that if $\phi(t; z)$ touches the threshold manifold $\mathcal{T}$ at $t = dT$, the point z will belong to S_0 or S_1 depending whether we apply the reset condition or not.

In this work we will mainly focus on orbits involving the sets S_0 and S_1. For this reason, we first show how to define $\mathfrak{s}$ in these sets. We refer to Fig. 1 in order to illustrate what follows.

If $z \in S_0$, no spike occurs and $\mathfrak{s}(z)$ becomes

$$\mathfrak{s}(z) = \mathfrak{s}_0(z) := \varphi_0(T - dT; \varphi_A(dT; z)), \tag{7}$$

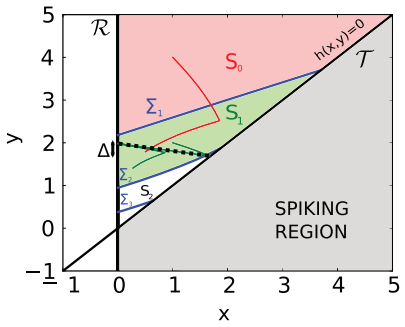

Fig. 1. Trajectories of system (22)–(24) with initial conditions in sets S_0 (red) and S_1 (green), plotted on top of the pieces S_0, S_1, S_2 where the stroboscopic map is defined. Boundaries Σ_1, Σ_2 and Σ_3 are computed using the algorithm described in Appendix A. Solid black curves correspond to the threshold manifold $\mathcal{T}$ and the reset manifold $\mathcal{R}$. Parameter values for the system are $c = 0.53$, $V_0 = 0.1$, $A = 2$, $\tau = 2$, $T = 3$, $\Delta = 0.3$ and $b = 0.1$. (For interpretation of the references to colour in this figure legend, the reader is referred to the web version of this article.)

where φ_A is the flow associated with the system $\dot{z} = f(z) + \nu A$.

In order to define the stroboscopic map in S_1, we consider the maps

$$P_1 : \begin{array}{ccc} \cup_{n\geq 1} S_n & \longrightarrow & \mathcal{T}\times\mathbb{T}_T \\ z & \longmapsto & (\varphi_A(t_*;z), t_*) \end{array} \tag{8}$$

$$\tilde{R} : \begin{array}{ccc} \mathcal{T}\times\mathbb{T}_T & \longrightarrow & \mathcal{R}\times\mathbb{T}_T \\ (z,t) & \longmapsto & (R(z),t) \end{array} \tag{9}$$

$$\tilde{P}_2 : \begin{array}{ccc} \mathcal{R}\times\mathbb{T}_T & \longrightarrow & \mathbb{R}^2 \\ (z,t) & \longrightarrow & \varphi_A(dT-t;z) \end{array} \tag{10}$$

$$P_3 : \begin{array}{ccc} \mathbb{R}^2 & \longrightarrow & \mathbb{R}^2 \\ z & \mapsto & \varphi_0(T-dT;z) \end{array} \tag{11}$$

where $\mathbb{T}_T := \mathbb{R}/T\mathbb{Z}$ and the symbol $\tilde{}$ emphasizes that the domain of the map involves time.

The map P_1 sends points in $\mathbb{D}$ to the threshold $\mathcal{T}$ by integrating the flow φ_A; it returns the hitting point on $\mathcal{T}$ and the time t_* needed by the trajectory to reach $\mathcal{T}$. In principle, to relate P_1 with system (1)–(3), its domain should be those points in $\mathbb{D}$ for which $0 < t_* \leq dT$, which is contained in $\cup_{n\geq 1} S_n$. However, the map P_1 can be extended to all points in $\mathbb{D}$ whose flow $\varphi_A(t;z)$ reaches the threshold for some $t_* > 0$, independently on whether $t_* \leq dT$ or not (see Section 3.2 for more details). This extension becomes specially useful for numerical purposes as well as to provide insight into the dynamics of the stroboscopic map near the switching manifolds.

The map $\tilde{R}$ is the reset map defined in (4) carrying on time. The map $\tilde{P}_2$ integrates the flow φ_A with initial condition at the reset manifold $\mathcal{R}$ for the remaining time until $t = dT$. Note that, similarly as for P_1, $\tilde{P}_2$ can also be extended outside its natural domain by letting $t < 0$ (see Section 3.2 for more details). Finally, the map P_3 is a truly stroboscopic map, which integrates the flow φ_0 for a fixed time $T - dT$.

Since by hypothesis *H.2*, spikes are only possible for $A > 0$ (that is, $0 < t_* \leq dT$), then, for $z \in S_1$, the stroboscopic map becomes

$$\mathfrak{s}(z) = \mathfrak{s}_1(z) := P_3 \circ \tilde{P}_2 \circ \tilde{R} \circ P_1(z). \tag{12}$$

By considering $\tilde{P}_1$ the extended version (to $\mathbb{R}^2 \times \mathbb{T}_T$) of the map P_1 and recalling that spikes can only occur for $0 < t \leq dT$, if $z \in S_n$, $n \geq 1$ the stroboscopic map becomes

$$\mathfrak{s}(z) = \mathfrak{s}_n(z) := P_3 \circ \tilde{P}_2 \circ \left(\tilde{R} \circ \tilde{P}_1\right)^{n-1} \circ \tilde{R} \circ P_1(z). \tag{13}$$

Then, the stroboscopic map can be written as the piecewise smooth discontinuous map:

$$\mathfrak{s}(z) = \begin{cases} \mathfrak{s}_0(z) & \text{if } z \in S_0 \\ \mathfrak{s}_n(z) & \text{if } z \in S_n,\ n \geq 1 \end{cases}$$

Remark 3. If one allows the system to exhibit spikes for $A = 0$ (i.e, hypothesis *H.2* is not satisfied), then the stroboscopic map can be similarly defined by reordering accordingly the sequence of maps $\tilde{P}_i$ and $\tilde{R}$ in Eq. (13). Moreover, the map $\mathfrak{s}$ restricted to S_n is still smooth as long as the sequence of maps is kept constant.

Remark 4. The stroboscopic map is discontinuous even if one identifies the threshold and the reset manifolds: $\mathcal{T} \sim R$. Although this would make trajectories of the flow continuous, the vector field (1) does not necessary coincide at the manifolds $\mathcal{T}$ and R and hence the stroboscopic map would still be discontinuous.

Let us now study the border, $\Sigma_1 \subset \mathbb{D}$, that separates the sets S_0 and S_1 and hence becomes a switching manifold of the stroboscopic map $\mathfrak{s}$ (see Fig. 1). This border is formed by the union of points whose trajectories graze the threshold manifold $\mathcal{T}$. Such a grazing can occur in two different ways defining two different types of points in Σ_1 :

(i) Smooth Grazing: points whose trajectory is tangent to $\mathcal{T}$.
(ii) Nonsmooth Grazing: points whose trajectory is transversal to $\mathcal{T}$ exactly for $t = dT$.

Provided that trajectories can only reach the threshold when $A > 0$, (condition *H.2*), nonsmooth grazing can only occur for $t = dT$, at times when the pulse $I(t)$ is disabled. However, trajectories may exhibit tangent grazing for $0 < t \leq dT$.

As mentioned above, the switching manifold Σ_1 can be split in two pieces according to *i)* and *ii)*:

$$\Sigma_1 = \Sigma_1^{\mathrm{S}} \cup \Sigma_1^{\mathrm{NS}},$$

where

$$\Sigma_1^{\mathrm{S}} = \Big\{ z \in \mathbb{D} \,|\, z = \varphi_A(t; z_0)\,, t \in [0, t_*], 0 < t_* \leq dT \ \text{ where } z_0 \text{ and } t_* \\ \text{are s.t. } h(\varphi_A(t_*; z_0)) = 0, \nabla h(\varphi_A(t_*; z_0)) \cdot \frac{d}{dt}\varphi_A(t_*; z_0) = 0 \Big\},$$

and

$$\Sigma_1^{\mathrm{NS}} = \{ z \in \mathbb{D} \,|\, h(\varphi_A(dT; z)) = 0 \}.$$

Remark 5. Similarly, one can define the boundaries Σ_i^{S} and Σ_i^{NS} with $i > 1$, which separate sets exhibiting more than one spike.

3.2. Virtual extension and contractiveness of the stroboscopic map

The maps $\mathfrak{s}_0$ and $\mathfrak{s}_1$ can (in some cases) be extended to their "virtual" domains, S_1 and S_0, respectively. In Section 6.2 we will show that the extended maps will be used to numerically compute feasible fixed points and bifurcation curves by means of a Newton method. Moreover, virtual extensions provide insight into the dynamics of the map in the actual domain. For instance, virtual attracting fixed points of the map suggest that the dynamics in the actual domain pushes trajectories towards them and therefore towards the switching manifold Σ_1.

Clearly, by ignoring the reset condition, one can always smoothly extend $\mathfrak{s}_0$ to S_1. That is, if $z \in S_1$, then we extend $\mathfrak{s}_0$ to S_1 by setting $\mathfrak{s}_0(z) = \varphi_0(t - dT; \varphi_A(dT; z))$, which is well defined. In words, "keep integrating system (1) with $I = A$ for a time dT even if the trajectory hits the threshold manifold $\mathcal{T}$".

Under certain conditions, one can also extend the map $\mathfrak{s}_1$ to S_0. Let $z \in S_0$ and assume that there exists $t_* > dT$ such that $\varphi_A(t_*; z) \in \mathcal{T}$. Then, although $z \notin S_1$, $\mathfrak{s}_1$ is also well defined at such a point by letting $t_* > dT$ in the definition of P_1 in (8) and using $t > dT$ when applying the map $\tilde{P}_2$ defined in (10), which will consist of integrating the flow φ_A backwards for $t = |dT - t_*|$. In words, "keep integrating system (1) with $I = A$ as much time as needed until the trajectory hits the threshold manifold $\mathcal{T}$ and reset. Then, integrate the flow of system (1) with $I = 0$ backwards in time the same amount time by which dT was exceeded". Note that, if $z \in S_0$ is close to Σ_1^{S}, then it may be that such t_* does not exist (the trajectory never hits the threshold manifold for $I = A$) and hence one cannot extend $\mathfrak{s}_1$ to S_0.

Regarding the contractiveness of $\mathfrak{s}$, we first discuss the map $\mathfrak{s}_0$ given in Eq. (7). Recalling that for $A = 0$ system (1) possesses a unique attracting equilibrium point in $\mathbb{D}$, this implies that φ_0 is contracting in $\mathbb{D}$. For $A > 0$ small, φ_A is also contracting. By contrast, for larger values of A, φ_A may be expanding in $\mathbb{D}$. If this is the case, this expansiveness can be compensated by integrating φ_0 for large enough time, $T - dT$, which occurs if dT is smaller enough than T so that we obtain

$$\left|\mathfrak{s}_0(z) - \mathfrak{s}_0(z')\right| < \left|z - z'\right|.$$

Regarding $\mathfrak{s}_1$, the spike exhibited by trajectories of point in S_1 may introduce expansiveness to $\mathfrak{s}_1$ (see Appendix B for the details on the computation of $D\mathfrak{s}_1$). Arguing similarly, this expansiveness can be compensated making dT smaller enough than T so that the contracting flow φ_0 is applied for large enough time.

4. Border collisions of fixed points of the stroboscopic map

By assumption *H.1*, for $A = 0$, system (1)–(3) possesses an attracting subthreshold equilibrium point, $z^* \in \mathbb{D}$. Although the periodic forcing $I(t)$ is not continuous in t, averaging theorem [25] holds, as the system is Lipschitz in z. This implies that, when $A > 0$ is small enough, system (1)–(3) possesses a T-periodic orbit, which is not differentiable at $t = 0 \pmod T$ and $t = dT \pmod T$ (recall that we assumed $t_0 = 0$). As its amplitude increases with A, this periodic orbit may undergo a *grazing bifurcation* [26,27] if it collides with the boundary $\mathcal{T}$ when varying A. This corresponds to a fixed point $\bar{z}_0 \in S_0$ of the stroboscopic map undergoing a *border collision bifurcation* [28] when colliding with Σ_1. In general, a bifurcation occurs when a fixed point $\bar{z}_n \in S_n, n \geq 1$ collides with Σ_{n+1} or Σ_n. Following *i)* and *ii)* of Section 3.1, we distinguish two different types of border collision bifurcations:

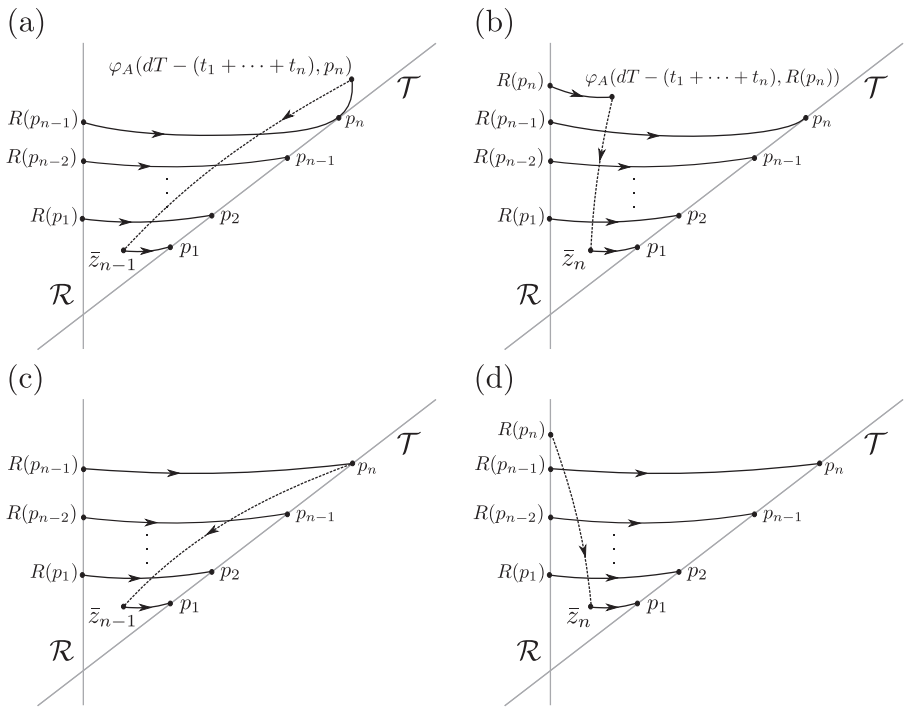

Fig. 2. Scheme showing a periodic orbit of the system (1)–(3) (a,b) grazing tangentially the manifold $\mathcal{T}$ at the point p_n and (c,d) grazing the manifold $\mathcal{T}$ at the non-differentiable point p_n at time dT. These periodic orbits correspond to fixed points of the stroboscopic map hitting the manifold Σ_n^S (a,b) and the manifold Σ_n^{NS} (c,d). Panels (a,c) correspond to a collision of a point $\bar{z}_{n-1} \in S_{n-1}$ with Σ_n, while panels (b,d) correspond to a collision of the point $\bar{z}_n \in S_n$ with Σ_n. See Section 4 for more details. Solid black lines correspond to trajectories of the flow φ_A, while dashed black lines correspond to trajectories of the flow φ_0. Grey lines correspond to the reset manifold $\mathcal{R}$ and the threshold manifold $\mathcal{T}$.

1. **Smooth grazing bifurcation**: the T-periodic orbit of system (1)–(3) grazes tangentially $\mathcal{T}$, and, equivalently, the fixed point of the stroboscopic map collides with Σ_n^S, for some $n \geq 1$. The fixed point can collide with Σ_n^S from two different regions, namely, S_{n-1} and S_n. When the fixed point $\bar{z}_{n-1} \in S_{n-1}$ collides with Σ_n^S, the following equations are satisfied (see Fig. 2(a)):

$$\bar{z}_{n-1} = \varphi_A(-t_1, p_1) = \varphi_0(T - dT, \varphi_A(dT - (t_1 + \cdots + t_n), p_n) \tag{14}$$

with

$$\begin{aligned} p_2 &= \varphi_A(t_2, R(p_1)) \\ p_3 &= \varphi_A(t_3, R(p_2)) \\ &\vdots \\ p_n &= \varphi_A(t_n, R(p_{n-1})) \end{aligned} \tag{15}$$

and

$$\begin{aligned} &(f(p_n) + \nu A) \cdot \nabla h(p_n) = 0 \\ &h(p_1) = h(p_2) = \ldots = h(p_n) = 0. \end{aligned} \tag{16}$$

While, when $\bar{z}_n \in S_n$ collides with Σ_n^S the equation is

$$\bar{z}_n = \varphi_A(-t_1, p_1) = \varphi_0(T - dT, \varphi_A(dT - (t_1 + \cdots + t_n), R(p_n)) \tag{17}$$

and the other conditions (15)–(16) as before (see Fig. 2(b)).

Remark 6. Notice that we assume that the smooth grazing with the manifold $\mathcal{T}$ occurs after the last spike (this will be the situation in the example considered in Section 6). In general, this is not necessary the case, and similar equations can be written for other situations.

2. **Nonsmooth grazing bifurcation**: the T-periodic orbit of system (1)–(3) grazes $\mathcal{T}$ at the non-differentiable point given by $t = dT$, and, equivalently, the fixed point of the stroboscopic map collides with Σ_n^{NS}, for some $n \geq 1$. The fixed point can collide with Σ_n^{NS} from two different regions, namely, S_{n-1} and S_n. When the fixed point $\bar{z}_{n-1} \in S_{n-1}$ collides with Σ_n^{NS}, the following equations are satisfied (see Fig. 2(c)):

$$\bar{z}_{n-1} = \varphi_A(-t_1, p_1) = \varphi_0(T - dT, p_n) \tag{18}$$

with

$$\begin{aligned} p_2 &= \varphi_A(t_2, R(p_1)) \\ p_3 &= \varphi_A(t_3, R(p_2)) \\ &\vdots \\ p_n &= \varphi_A(dT - (t_1 + \cdots + t_{n-1}), R(p_{n-1})) \end{aligned} \tag{19}$$

and

$$h(p_1) = h(p_2) = \ldots = h(p_n) = 0. \tag{20}$$

While, when $\bar{z}_n \in S_n$ collides with Σ_n^{NS} the equation is

$$\bar{z}_n = \varphi_A(-t_1, p_1) = \varphi_0(T - dT, R(p_n)) \tag{21}$$

and the other conditions (19)–(20) as before (see Fig. 2(d)).

In Section 6 we compute (for a particular example) the critical parameter values at which the fixed points $\bar{z}_0$ and $\bar{z}_1$ undergo border collision bifurcations when colliding with Σ_1 and Σ_2 (the latter, only for $\bar{z}_1$) by means of solving numerically (using a Newton method) the systems of equations given above.

After a border collision bifurcation of a fixed point in S_n colliding with $\Sigma_{n+1}^{\mathrm{NS}}$, it is expected that the map will map points in S_n to points in S_{n+1} and viceversa, thus causing the dynamics to alternate between S_n and S_{n+1}. Therefore, it is possible that there appear periodic orbits of the stroboscopic map hitting both regions S_n and S_{n+1}. In the next section, we will provide techniques to study such periodic orbits.

5. Periodic orbits of the stroboscopic map

Beyond the fixed points, we also study periodic orbits of the stroboscopic map $\mathfrak{s}$. Assume that the fixed point $\bar{z}_n$ of $\mathfrak{s}$ collides with $\Sigma_{n+1}^{\mathrm{NS}}$ for some parameter value undergoing a border collision bifurcation as described in Section 4. In this situation, $\mathfrak{s}$ may possess periodic orbits visiting both S_n and S_{n+1}. Unfortunately, there is little general theory that can be applied to prove the existence of such periodic orbits. In this section, we review possibly the only result (to our knowledge) in this direction by Gambaudo et al. We first introduce symbolic dynamics and some definitions in order to characterize these periodic orbits.

Definition 1. Given $z \in S_n \cup S_{n+1}$, we define the itinerary of z by $\mathfrak{s}$ as

$$I_{\mathfrak{s}}(z) = \left(a(z), a(\mathfrak{s}(z)), a\left(\mathfrak{s}^2(z)\right), \ldots\right),$$

where

$$a(z) = \begin{cases} 1 & \text{if } z \in S_{n+1} \\ 0 & \text{if } z \in S_n. \end{cases}$$

Remark 7. Although we consider only periodic orbits that interact with two regions (S_n and S_{n+1}), it is possible to extend the results and definitions to orbits interacting with more than two regions. However, this situation is out of scope of our paper.

Definition 2. One calls $W_{p,\,q}$ the set of periodic symbolic sequences generated by infinite concatenation of a symbolic block of length q containing p symbols 1:

$$W_{p,q} = \left\{\mathbf{y} \in \{0,1\}^{\mathbb{N}} \,|\, \mathbf{y} = \mathbf{x}^{\infty},\ \mathbf{x} \in \{0,1\}^q \text{ and } \mathbf{x} \text{ contains } p \text{ symbols } 1\right\}.$$

Definition 3. One says that a sequence in $W_{p,\,q}$ has rotation number p/q.

Remark 8. In the one-dimensional case, this definition of the rotation number coincides with the classical one for one-dimensional circle maps through a lift (see [19]). However, in the planar case, it becomes in general difficult (if possible) to define this number by means of lifts, as the dynamics cannot always be reduced to a 2-dimensional torus. However, following [24,29], we abuse notation and call this number the "rotation number".

Definition 4. Symbolic sequences can be ordered using that $0 < 1$. Hence,

$$(\mathbf{x}_1\mathbf{x}_2\ldots) < (\mathbf{y}_1\mathbf{y}_2\ldots)$$

if and only if $\mathbf{x}_1 = 0$ and $\mathbf{y}_1 = 1$ or $\mathbf{x}_1 = \mathbf{y}_1$ and there exists some $j > 1$ such that

$$\mathbf{x}_i = \mathbf{y}_i, \text{ for all } i < j$$
$$\mathbf{x}_j = 0$$
$$\mathbf{y}_j = 1.$$

This order allows one to consider the following definition:

Definition 5. Let σ be the shift operator. One says that a symbolic sequence $\mathbf{x} \in W_{p,\,q}$ is maximin if

$$\min_{0\le k\le q}\left(\sigma^k(\mathbf{x})\right) = \max_{\mathbf{y}\in W_{p,q}}\left(\min_{0\le k\le q}\left(\sigma^k(\mathbf{y})\right)\right).$$

Example 1. Up to cyclic permutations, there exist only two periodic sequences in $W_{2,\,5}$, which are represented by means of two blocks that, when expressed in minimal form, are given by $0^3 1^2$ and $0^2 101$. The maximum of the minimal blocks is $0^2 101$, therefore the symbolic sequence generated by $0^2 101$ is maximin.

Intuitively, maximin symbolic sequences have "well" distributed symbols 1 along the sequence, which is related to the notion of "well ordered" symbolic sequences (see Definition 6).

Alternatively, maximin itineraries can be defined as those belonging to the Farey tree of symbolic sequences. This means that they are given by concatenation of two maximin sequences such that their rotation numbers are Farey neighbours. See [19] for a recent review in this topic.

Then, we may apply the following result to study the existence of maximin periodic orbits:

Theorem 1 (Dynamics of quasi-contractions)**.** *Assume that there exist sets $E_0 \subset S_n$ and $E_1 \subset S_{n+1}$ such that*

(i) $\mathfrak{s}(E_i) \subset E_0 \cup E_1$, *for* $i = 0, 1$.
(ii) $\mathfrak{s}_0$ *and* $\mathfrak{s}_1$ *contract in* E_0 *and* E_1, *respectively.*
(iii) $\mathfrak{s}^i(\Sigma^{\mathrm{NS}}) \cap \Sigma^{\mathrm{NS}} = \emptyset$ *for all* $i \ge 1$.

Then, provided that $\mathfrak{s}$ preserves orientation, $\mathfrak{s}$ possesses 0 or 1 periodic orbit. In the latter case, its itinerary is maximin.

The previous result was stated in [29] for quasi-contractions in metric spaces and adapted in [19] for piecewise continuous contracting maps in $\mathbb{R}^n$.

Remark 9. The previous theorem establishes the existence of 0 or 1 periodic orbits when the map preserves orientation. For the one-dimensional case, an orientation-preserving quasi-contraction can be seen as a contracting circle map, which possesses 0 periodic orbits when its rotation number is irrational. In this case, its ω-limit consists of a Cantor set or the whole circle, and this occurs only for a set of parameter values of zero measure (see [19] for the details). However, for the higher-dimensional case, this is still an open problem to understand how large is the set of parameter values leading to 0 periodic orbits and how is the dynamics when this occurs. Therefore, for our purposes, this theorem will be useful only to show that, if a periodic orbits exists, it has to have a maximin itinerary.

In Section 6.3 we will show how Theorem 1 can be applied to a particular example to prove that, if a periodic orbit exists, its itinerary must be maximin by checking the hypothesis using semi-rigorous numerics.

6. Application to a neuron model

In this section, we apply the theoretical results presented in previous sections to a spiking neuron model of integrate-and-fire type with a dynamic threshold.

6.1. The model

We consider the system proposed in [6], which consists of a leaky integrate-and-fire model with a dynamic threshold. It is a dimensionless version of other similar models such as [4,5]. The system is submitted to periodic forcing $I(t)$ as in Eq. (2). The equations are given by:

$$\begin{aligned} \dot{V} &= -V + V_0 + I(t) \\ \tau_\theta \dot{\theta} &= -\theta + \theta_\infty(V) \end{aligned} \tag{22}$$

where $(V, \theta) \in \mathbb{R}^2$ are the neuron voltage and the threshold, respectively. The function

$$\theta_\infty(V) = a + e^{b(V-c)} \tag{23}$$

is the steady state value of the threshold θ, with $a, b, c \in \mathbb{R}$; τ_θ is the time constant for the threshold (which will be chosen only a bit slower than the membrane time constant, i.e. $\tau_\theta > 1$) and V_0 is the voltage at the resting state. The spiking reset rule is given by:

$$\text{if } V(t_*) = \theta(t_*) \text{ then } V(t_*^+) = V_r \text{ and } \theta(t_*^+) = \theta(t_*) + \Delta, \tag{24}$$

with V_r and Δ being real parameters. Following [6], the parameters of the system along this paper are $V_0 = 0.1$, $V_r = 0$, $\Delta = 0.3$, $a = 0.08$, $c = 0.53$ and $\tau_\theta = 2$. Parameter b will vary along this study between 0 and 1. The rest of parameters, d, T and A, describe the input. In this work, parameter d will be fixed to $d = 0.5$, and T and A will take different values leading to different dynamics as discussed in Sections 6.2–6.4.

Notice that system (22)–(24) is of the form (1)–(3), with a threshold manifold

$$\mathcal{T} = \left\{(V,\theta) \in \mathbb{R}^2 \,|\, h(V,\theta) = V - \theta = 0\right\},$$

reset map

$$R: \begin{array}{ccc} \mathcal{T} & \longrightarrow & \mathcal{R} \\ (V,\theta) & \longmapsto & (V_r, \theta + \Delta), \end{array}$$

reset manifold

$$\mathcal{R} = \left\{(V,\theta) \in \mathbb{R}^2 \,|\, V = V_r\right\},$$

and subhtreshold domain

$$\mathbb{D} = \{(V,\theta),\ |\, V \geq V_r,\ V < \theta\}.$$

Notice that for biological reasons we restrict the subthreshold domain to $V \geq V_r$. Hence, the subthreshold domain is the region in the first quadrant between the vertical line $V = V_r$ and the diagonal $V = \theta$, as shown in Fig. 1 for $V_r = 0$.

Next we show that system (22) satisfies hypothesis *H.1* and *H.2*. Indeed, for $A = 0$, the system has a subthreshold equilibrium point at $(V^*, \theta^*) = (V_0, \theta_\infty(V_0)) \in \mathbb{D}$ (it satisfies $V_0 < \theta_\infty(V_0)$ for the choice of parameters) with eigenvalues $\lambda_1 = -1$ and $\lambda_2 = -1/\tau_\theta$. Thus, it is an attracting node. The associated eigenvectors are $v_1 = (1, \theta'_\infty(V^*)/(1-\tau_\theta))$ and $v_2 = (0,1)$, respectively. Then, assuming that $\tau_\theta > 1$, trajectories approach the equilibrium point tangentially to the V-nullcline ($V = V_0$). This guarantees the existence of trajectories staying in $\mathbb{D}$ as along as desired without intersecting the diagonal, $\mathcal{T}$.

In order to prove hypothesis *H.2* we will show that the vector field on the threshold manifold $\mathcal{T}$ points towards $\mathbb{D}$. Therefore, we need to impose that the vector $(-V + V_0, -V + \theta_\infty(V))$ satisfies $-V + \theta_\infty(V) > -V + V_0$, which implies $\theta_\infty(V) > V_0$. Thus, choosing parameters *a, b, c* such that $\theta_\infty(V) > V_0$ for all values of V (i.e. $\theta_\infty(V) > a + e^{-b(V_r - c)} > V_0$), we have that all points in $\mathbb{D}$ belong to orbits that do not intersect $\mathcal{T}$ for $A = 0$.

Remark 10. If one choses a function $\theta_\infty(V)$ for which hypothesis H.2 is not satisfied, the mathematical analysis presented in Sections 2–4 still follows if $z^* = (V^*, \theta^*)$ is enough isolated from those points not satisfying hypothesis *H.2*. In this case, one can safely remove these points from $\mathbb{D}$ and the analysis in the mentioned sections holds nevertheless.

6.2. Fixed points and their bifurcations

In this section we analyze the bifurcations of the fixed points of the stroboscopic map (corresponding to T-periodic orbits of the time-continuous system (22)–(24)) when varying parameters of the system. We focus on bifurcations exhibited by the fixed points $\bar{z}_0 \in S_0$ and $\bar{z}_1 \in S_1$, as they are more relevant from an applied point of view, given that they combine spiking and subthreshold dynamics. A similar analysis can be done for fixed points exhibiting more spikes, $\bar{z}_n \in S_n$. We focus on bifurcations associated to piecewise smooth maps (border collisions), although other bifurcations of smooth maps such as the Neimark-Sacker bifurcation may occur. As explained in Section 4, such border collision bifurcations correspond to a periodic orbit of the time-continuous system grazing the threshold, which can occur through a tangency (smooth grazing or, equivalently, border collision with Σ_1^S or Σ_2^S) or when disabling the pulse (nonsmooth grazing or, equivalently, border collision with Σ_1^{NS} or Σ_2^{NS}).

One of the characteristics of system (22) which may influence having smooth or nonsmooth grazing bifurcations is the position of the equilibrium point for $I = A$ (given by the intersection of the nullclines, which occurs at $V^* = V_0 + A$ and $\theta^* = \theta_\infty(V_0 + A)$). If this point happens to be far away from the domain $\mathbb{D}$ ($V \gg \theta$), then the dynamics is fast, trajectories spend little time between spikes and transversal grazing is most likely to occur. However, if the equilibrium point is close to the threshold manifold (or even at $\mathbb{D}$), then the dynamics is slower and system may exhibit tangencies with $\mathcal{T}$. The nature of the function $\theta_\infty(V)$ allows these two situations mainly by varying the parameter b between 0 and 1. For small b (close to 0) the nullcline $\theta = \theta_\infty(V)$ becomes almost flat in $\mathbb{D}$ and fixes the equilibrium point for $I = A$ outside $\mathbb{D}$ (see Figs. 3(a) and (b)). However, for larger values of b the function $\theta_\infty(V)$ may be completely located in $\mathbb{D}$ (see Figs. 3(c) and (d)). Moreover, the latter case has consequences from the neuron modeling point of view as these systems are not capable to show repetitive firing for constant input and they are referred as phasic neurons [7].

Apart from A and b, other relevant parameters influencing these different type of behaviours are T and d, as they control the integration time during the active part of the pulse. When the pulse is active for a short time, the regions S_n, $n > 1$, occupy a small portion of the subthreshold domain (see Figs. 3(b) and (d)). In this work we keep $d = 0.5$ fixed, and study bifurcations of the fixed points $\bar{z}_0$ and $\bar{z}_1$ when varying *b, A* and *T*.

We first fix $T = 0.5$ and compute the bifurcation curves of the fixed points $\bar{z}_0$ and $\bar{z}_1$ in the parameter space (b, A) (see Fig. 4). These curves have been computed semi-analytically using a predictor-corrector method detailed in Appendix C. As we are computing periodic orbits close to bifurcations, the method may predict or correct a point outside the feasible domain. However, as explained in Section 3.2, the system can be extended to virtual domains and allow the Newton method to continue and converge.

In black we show the border collision curve given by the collision of the fixed point $\bar{z}_0 \in S_0$ with Σ_1^{NS} (nonsmooth grazing). Recall that at this bifurcation a non-spiking T-periodic orbit grazes the threshold precisely when the pulse is disabled

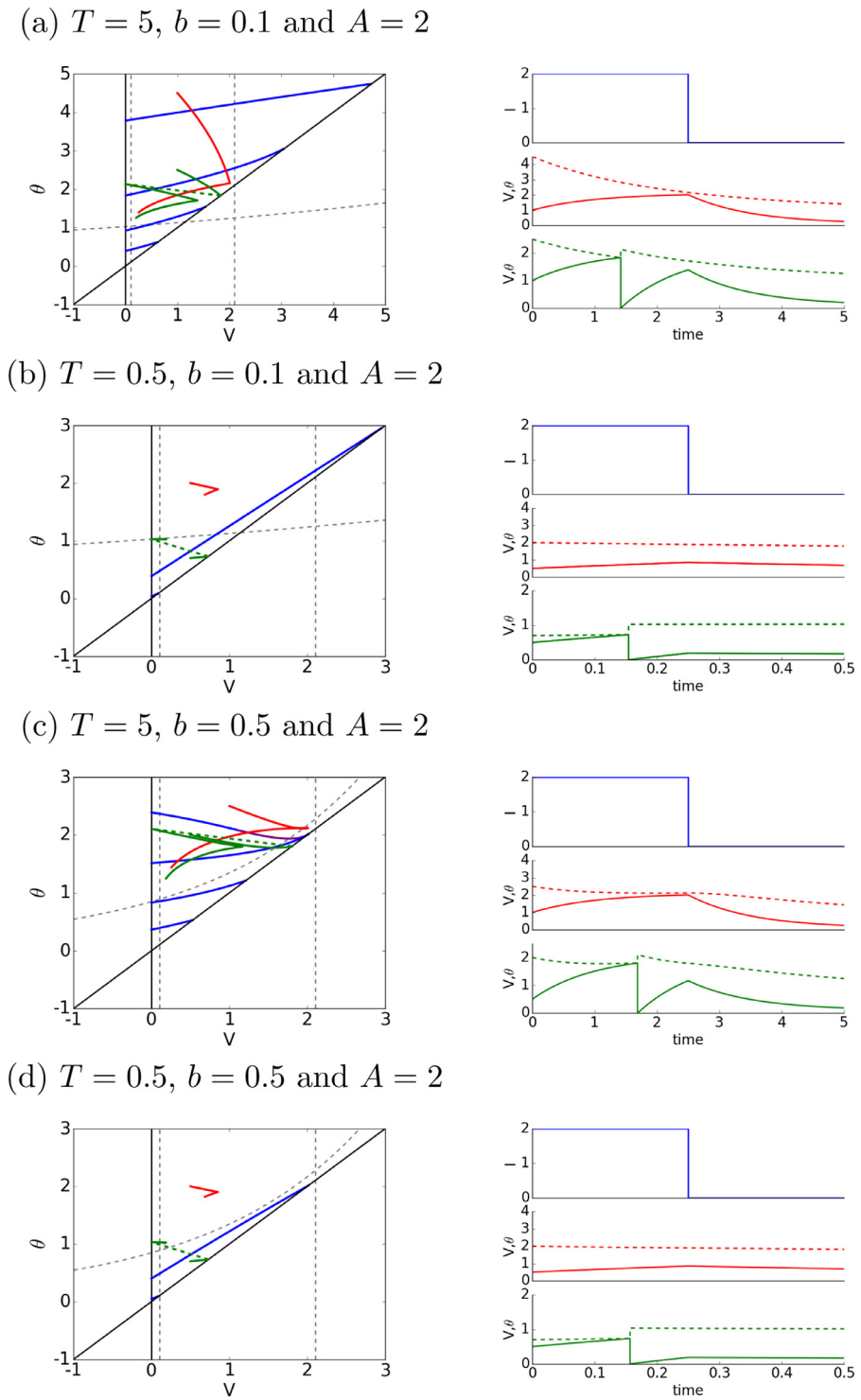

Fig. 3. (Left) Trajectories of system (22)–(24) on the (V, θ) phase space with initial conditions in sets S_0 (red) and S_1 (green). Blue curves correspond to the boundaries Σ_n^{NS}, $n \geq 1$ and the purple curve to the boundary Σ_1^S. Gray dashed curves correspond to θ- and V-nullclines for $I = 0$ and $I = A$; and their intersection corresponds to the point (V^*, θ^*). Solid black curves correspond to the reset manifold $\mathcal{R}$ and the threshold manifold $\mathcal{T}$. (Right) Times courses of $I(t)$ and the variables V (solid) and θ (dashed) for the trajectories shown on the left with the same color. (For interpretation of the references to colour in this figure legend, the reader is referred to the web version of this article.)

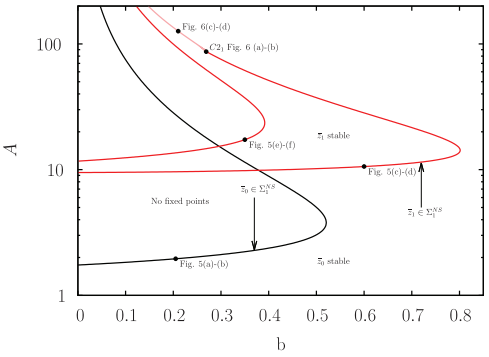

Fig. 4. Border collision bifurcation curves and regions of existence of $\bar{z}_0$ and $\bar{z}_1$ in the (b, A) parameter space for $T = 0.5$ (vertical axis is in logarithmic scale). Curve in black corrsponds to a border collision of $\bar{z}_0 \in S_0$ with Σ_1^{NS}. Curve in dark red corresponds to a border collision of $\bar{z}_1 \in S_1$ with Σ_1^{NS} (outer curve) and Σ_2^{NS} (inner curve). Curve in light red corresponds to a border collision of $\bar{z}_1 \in S_1$ with Σ_1^{S}. Dots on these curves indicate the parameter values (A, b) for which we show (in the Figure indicated nearby) the trajectory of the periodic orbit of the time continuous system that undergoes a grazing bifurcation. (For interpretation of the references to colour in this figure legend, the reader is referred to the web version of this article.)

(see Figs. 5(a) and 5(b)). Hence, as detailed in Appendix C, this curve has been computed numerically solving Eqs. (18)–(20) for $n = 1$ which, in this particular case, become

$$\varphi_A(-dT; (V, V)) = \varphi_0(T - dT; V, V), \tag{25}$$

where V, b and A are the unknowns. Crossing this curve with increasing A, the fixed point $\bar{z}_0$ first disappears and reappears again, as the curve exhibits a fold. For the given value of T, $\bar{z}_0$ does not exhibit any border collision involving Σ_1^S.

In red we show two border collision curves. The outer one corresponds to the collision of the fixed point $\bar{z}_1 \in S_1$ with Σ_1^{NS} (nonsmooth grazing), which corresponds to a spiking T-periodic orbit grazing the threshold precisely when the pulse is disabled (see Figs. 5(c) and 5(d)). This curve has been computed numerically solving Eqs. (19)–(21) for $n = 1$ which, in this particular case, become

$$\varphi_A(-dT; (V, V)) = \varphi_0(T - dT; V_r, V + \Delta), \tag{26}$$

where V, b and A are the unknowns.

The outer red bifurcation curve stops at a point labeled as $C2_1$. At this point, the grazing bifurcation occurring at $t = dT$ becomes smooth (see Figs. 6(a) and 6(b)). This point is hence a co-dimension-two bifurcation point as both smooth and nonsmooth grazing bifurcation conditions (Eqs. (15)–(17) and (19)–(21) for $n = 1$) are simultaneously satisfied. From this point on, the fixed point $\bar{z}_1$ collides with Σ_1^S, which corresponds to the light red bifurcation curve in Fig. 4. Recall that at this bifurcation a spiking T-periodic orbit tangentially grazes the threshold $\mathcal{T}$ (see Figs. 6(c) and 6(d)). This curve has been computed numerically solving Eqs. (15)–(17) for $n = 1$ which, in this particular case, become

$$\varphi_A(-t_1; (V, V)) = \varphi_0(T - dT; \varphi_A(dT - t_1; V_r, V + \Delta) \tag{27}$$

$$-V + V_0 + A = \frac{-V + \theta_\infty(V)}{\tau_\theta}, \tag{28}$$

where V, t_1, b and A are the unknowns.

The inner red curve corresponds to the collision of the fixed point $\bar{z}_1$ with Σ_2^{NS}, which corresponds to a spiking T-periodic orbit which attempts to exhibit a new spike by grazing the threshold precisely when the pulse is disabled (see Figs. 5(e) and 5(f)). As detailed in Appendix C, this curve has been computed numerically solving Eqs. (18)–(20) for $n = 2$ which, in this particular case, become

$$\begin{aligned} &\varphi_A(-t_1; (V_1, V_1)) = \varphi_0(T - dT; V_2, V_2) \\ &\qquad (V_2, V_2)^T = \varphi_A(dT - t_1; V_r, V_1 + \Delta), \end{aligned} \tag{29}$$

where V_1, V_2, t_1, b and A are the unknowns.

For the given value of T, $\bar{z}_1$ does not exhibit any border collision involving Σ_2^S.

In the region limited by the inner and outer red curves defining the bifurcations $\bar{z}_1 \in \Sigma_2$ and $\bar{z}_1 \in \Sigma_1$, respectively, the fixed point $\bar{z}_1 \in S_1$ exists. Note also that the curves defined by $\bar{z}_0 \in \Sigma_1^{NS}$ and $\bar{z}_1 \in \Sigma_1^{NS}$ (black and outer dark red curves) cross transversally. This implies the existence of a region where both fixed points $\bar{z}_0$ and $\bar{z}_1$ coexist and are stable, as well as the existence of a region where, none of the fixed points $\bar{z}_0$ and $\bar{z}_1$ exist. Instead, one finds higher periodic orbits organized by period adding-like structures, which will be treated in more detail in Section 6.3.

In Fig. 7 we show the results of a similar analysis for $T = 5$. We observe the same nonsmooth grazing bifurcations as for $T = 0.5$ but this case shows more smooth grazing bifurcations. Thus, we do not repeat the details for the nonsmooth grazing bifurcations that have already been discussed and we focus on the new ones.

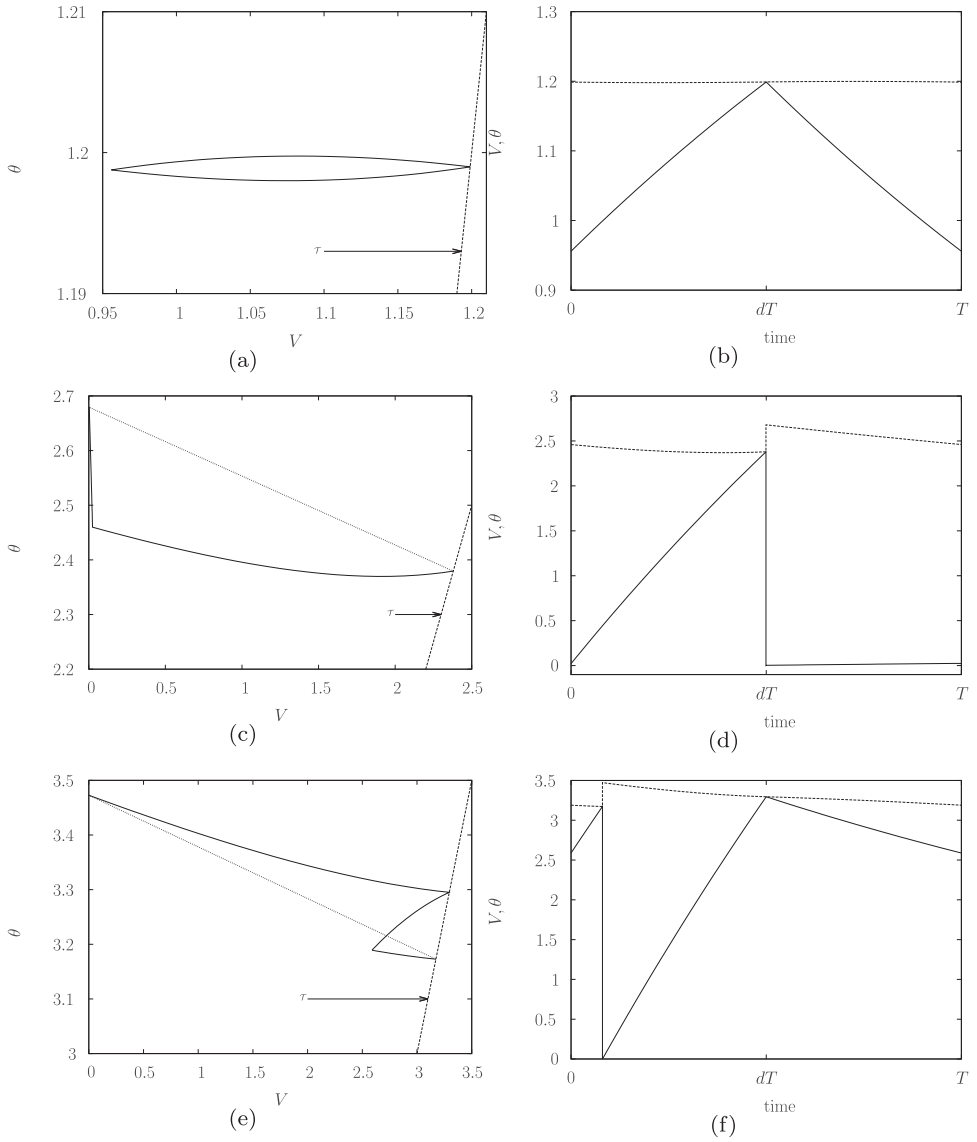

Fig. 5. Trajectories of T-periodic orbits undergoing the grazing bifurcations labeled in Fig. 4. (a,b) Nonsmooth grazing bifurcation of a non-spiking periodic orbit (border collision of $\bar{z}_0 \in S_0$ with Σ_1^{NS}). (c,d) Nonsmooth grazing bifurcation of a 1-spiking periodic orbit (border collision of $\bar{z}_1 \in S_1$ with Σ_1^{NS}). (e,f) Nonsmooth grazing bifurcation of a 1-spiking periodic orbit (border collision of $\bar{z}_1 \in S_1$ with Σ_2^{NS}). Left panels show trajectories on the (V, θ)-phase space while right panels show the corresponding time courses of the variables V (solid line) and θ (dashed line) over 1 period.

We observe that for $T = 5$ the fixed point $\bar{z}_0 \in S_0$ undergoes border collision bifurcations through smooth grazing, $\bar{z}_0 \in \Sigma_1^{\mathrm{S}}$. That is, a non-spiking T-periodic orbit tangencially grazes the threshold $\mathcal{T}$ (see Figs. 8(a) and 8(b)). The corresponding bifurcation curve is shown in gray in Fig. 7, and it has been computed solving Eqs. (14)–(16) for $n = 1$ which, in this particular case, become

$$\varphi_A(-t_1; (V, V)) = \varphi_0(T - dT; \varphi_A(dT - t_1; (V, V)))$$
$$-V + V_0 + A = \frac{-\theta + \theta_\infty(V)}{\tau_\theta},$$

where V, t_1, b and A are the unknowns.

We also observe that the fixed point $\bar{z}_1 \in S_1$ undergoes border collision bifurcations when colliding with Σ_2^{S}. We recall that, at this bifurcation a T-periodic orbit exhibing one spike reaches the threshold a second time by tangential grazing (see Fig. 8(c) and 8(d)). This bifurcation curve, shown in light red in Fig. 7, has been computed solving Eqs. (14)–(16) for $n = 2$

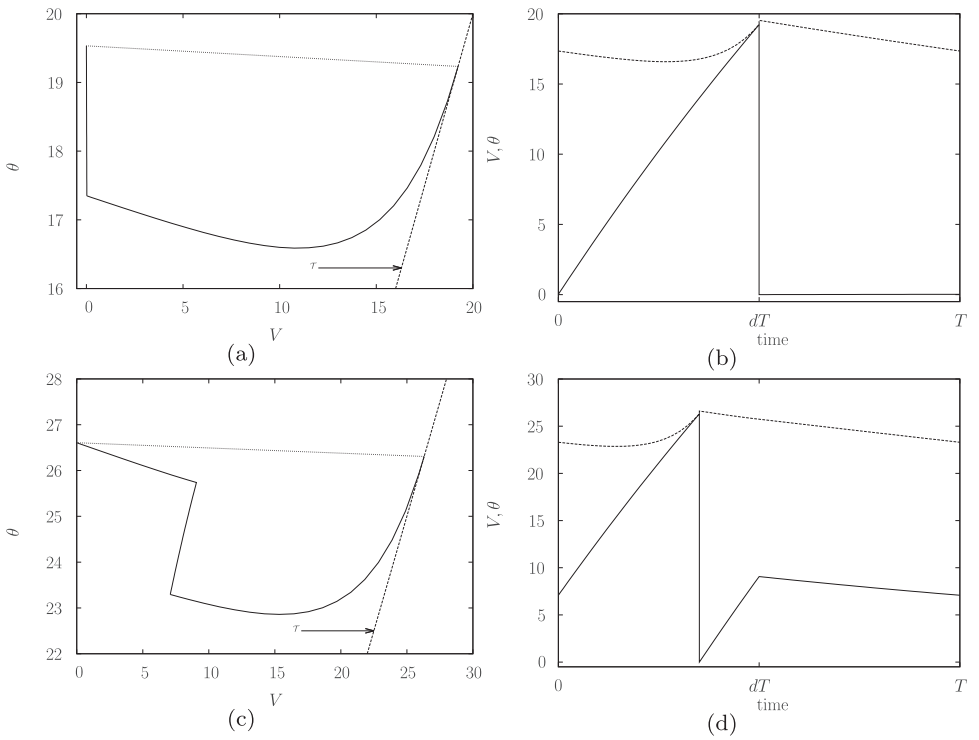

Fig. 6. Trajectories of T-periodic orbits undergoing the grazing bifurcations labeled in Fig. 4. (a,b) Co-dimension two bifurcation labeled as $C2_1$ in Fig. 4; a periodic orbit undergoes a smooth bifurcation at $t = dT$ ($\bar{z}_1 \in S_1$ collides with Σ_1^{NS} and Σ_1^{S} simultaneously). (c,d) Smooth grazing bifurcation of a 1-spiking periodic orbit (border collision of $\bar{z}_1 \in S_1$ with Σ_1^{S}.) Left panels show trajectories on the (V, θ)-phase space while right panels show the corresponding time courses of the variables V (solid line) and θ (dashed line) over 1 period.

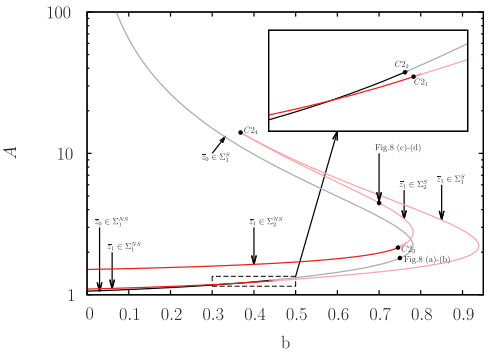

Fig. 7. Border collision bifurcation curves and regions of existence of the fixed points $\bar{z}_0$ and $\bar{z}_1$ in the (b, A) parameter space for $T = 5$ (vertical axis in logarithmic scale). Curves in black and gray correspond to border collision bifurcations of $\bar{z}_0 \in S_0$ with Σ_1^{NS} and Σ_1^{S}, respectively. Curves in red and light red correspond to border collision bifurcations of $\bar{z}_1 \in S_1$ with Σ^{NS} and Σ^{S}, respectively. Co-dimension-two bifurcation points are labeled as $C2_i$, $i = 2, 3, 4$ and are explained in the text. Dots on these curves indicate the parameter values (A, b) for which we show (in the Figure indicated nearby) the trajectory of the periodic orbit of the time continuous system that undergoes a grazing bifurcation. (For interpretation of the references to colour in this figure legend, the reader is referred to the web version of this article.)

which, in this particular case, become

$$\begin{aligned} \varphi_A(-t_1; V_1, V_1) &= \varphi_0(T - dT; \varphi_A(dT - t_2 - t_1; V_2, V_2)) \\ (V_2, V_2)^T &= \varphi_A(t_2; V_r, V_1 + \Delta) \\ -V_2 + V_0 + A &= \frac{-V_2 + \theta_\infty(V_2)}{\tau_\theta}, \end{aligned} \tag{30}$$

where V_1, V_2, t_1, t_2, b and A are the unknowns.

For $T = 5$ we observe 3 new co-dimension-two bifurcation points apart from the one reported in the case $T = 0.5$, $C2_1$. As for $C2_1$, two of these new points are given by the transition from nonsmooth to smooth grazing bifurcations. The curve

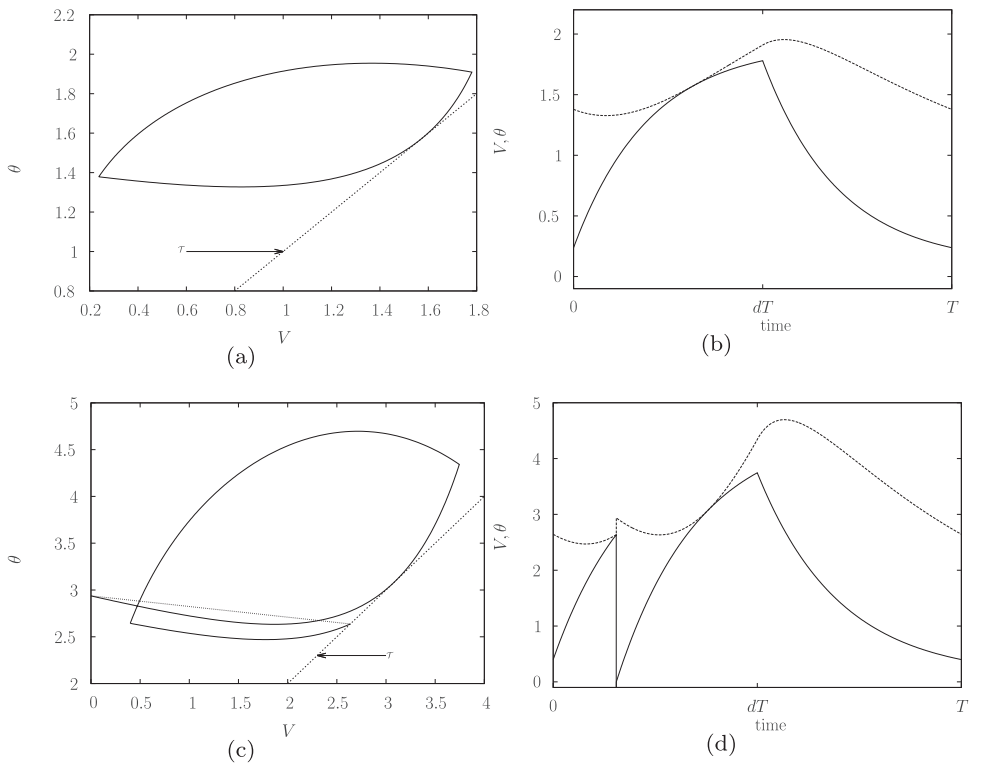

Fig. 8. Trajectories of T-periodic orbits undergoing the smooth grazing bifurcations labeled in Fig. 7. (a,b) Smooth grazing bifurcation of a non-spiking periodic orbit (border collision of $\bar{z}_0 \in S_0$ with Σ_1^S). (c,d) Smooth grazing bifurcation of 1-spiking periodic orbit (border collision of $\bar{z}_1 \in S_1$ with Σ_2^S).

defined by $\bar{z}_0 \in \Sigma_1$ transitions from $\bar{z}_0 \in \Sigma_1^{NS}$ (black curve) to $\bar{z}_0 \in \Sigma_1^S$ (gray curve) at the point labeled as $C2_2$ (see zoomed box in Fig. 7). At this point, both Eqs. (14)–(16) and (18)–(20) are simultaneously satisfied for $n = 1$ and hence this is a co-dimension-two bifurcation point. At these parameter values a non-spiking T-periodic orbit tangentially grazes the threshold at $t = dT$ (see Figs. 9(a) and 9(b)). Something similar occurs with the fixed point $\bar{z}_1 \in S_1$: a grazing bifurcation transitions from nonsmooth (dark red) to smooth type (light red) at the point $C2_3$ ($\bar{z}_1 \in \Sigma_2^{NS} \cap \Sigma_2^S$). At this point, both Eqs. (14)–(16) and (18)–(20) are simultaneously satisfied for $n = 2$ and hence this is a co-dimension-two bifurcation point. At these parameter values a T-periodic orbit exhibiting one spike grazes a second time the threshold at $t = dT$, and does it tangencially (see Figs. 9(c) and 9(d)).

The third co-dimension-two bifurcation point, $C2_4$, is of different type. Indeed, it is given by the intersection of the bifurcation curves defined by $\bar{z}_1 \in \Sigma_1^S$ and $\bar{z}_1 \in \Sigma_2^S$. At these parameter values a T-periodic orbit tangentially grazes the threshold twice (see Figs. 9(e) and 9(f)).

As in the previous case, the curves defined by $\bar{z}_0 \in \Sigma_1^{NS}$ and $\bar{z}_1 \in \Sigma_1^{NS}$ cross transversally defining four regions in the parameter space regarding their existence. In two of them only one fixed point exists (either $\bar{z}_0$ or $\bar{z}_1$), in another one both coexist and in the fourth one none of them exist. In the latter region one finds higher periodic orbits (see Section 6.3). In the case where both fixed points coexist one finds bi-stability, as both are attracting.

6.3. Periodic orbits of the stroboscopic map and bifurcations

In the previous section we have found the curves on the parameter space (b, A) where the fixed points $\bar{z}_0$ and $\bar{z}_1$ of the stroboscopic map $\mathfrak{s}$ undergo border collision bifurcations. As $\bar{z}_0$ and $\bar{z}_1$ collide with Σ_1 and disappear there might appear periodic orbits of the map visiting both S_0 and S_1. In order to explore the existence of such periodic orbits, we consider a set of initial conditions on the subthreshold regime (regions S_0 and S_1) and integrate them for several periods to identify the attracting periodic orbits of the system stepping on S_0 and S_1. See Appendix D for the numerical details. Of course, the same exploration can be done for orbits stepping on S_n, $n \geq 2$, but for the purposes of this paper we focus only on S_0 and S_1.

For $T = 0.5$ we computed the number of attracting periodic orbits of the stroboscopic map (see Fig. 10(a)) and their periods (see Fig. 10(b)). Notice that several periodic orbits coexist for many parameter values. Hence, whenever there are several periodic orbits the colour in Fig. 10(b) has been modified in order to reproduce the effect of the intersection. As with the fixed point $\bar{z}_1$, periodic orbits $(z_1, \ldots, z_n) \in (S_0 \cup S_1)^n$ of the stroboscopic map appear and disappear due to collisions

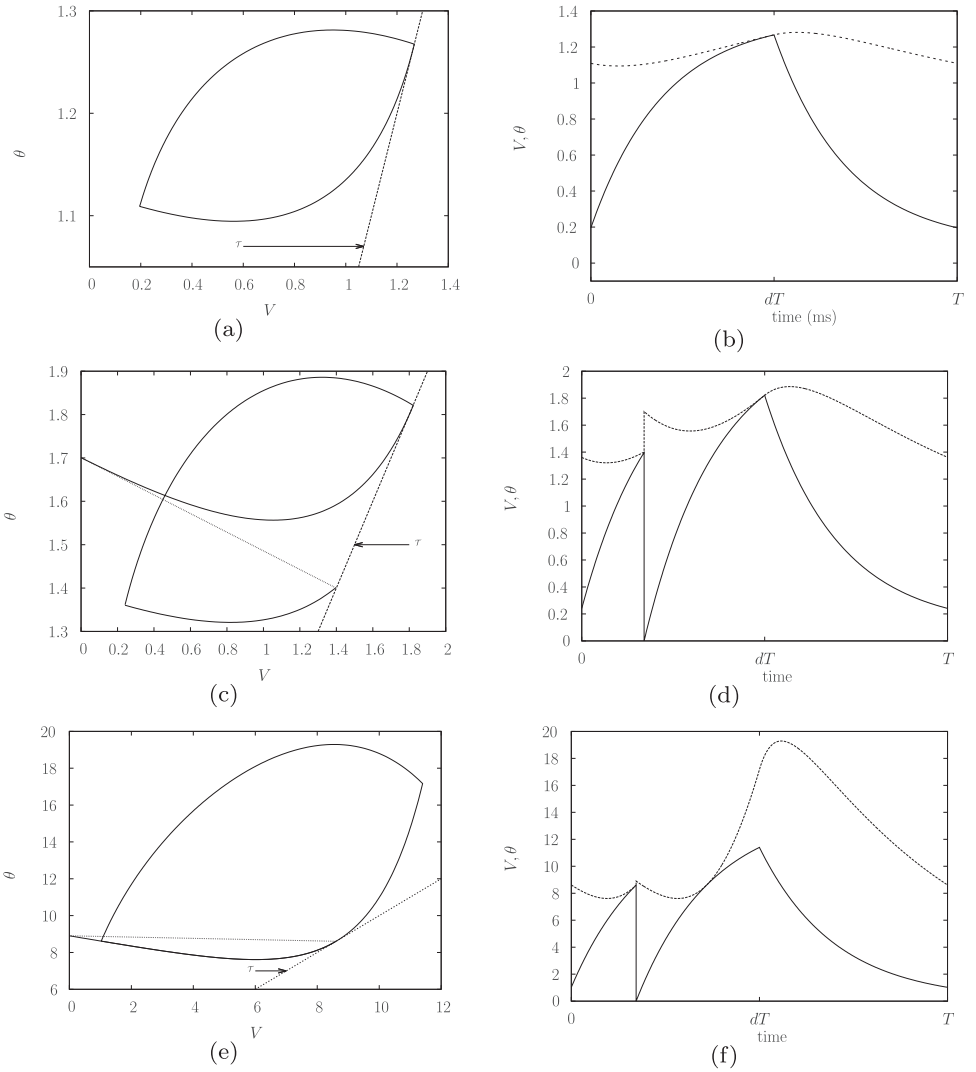

Fig. 9. Trajectories of the T-periodic orbits at the co-dimension two bifurcation points labeled in Fig. 7. (a,b) Point $C2_2$: a non-spiking periodic orbit tangentially grazes the threshold at $t = dT$ ($\tilde{z}_0 \in \Sigma_1^{NS} \cap \Sigma_1^{S}$). (c,d) Point $C2_3$: a 1-spiking periodic orbit tangencially grazes the threshold precisely at $t = dT$, when the pulse is disabled ($\tilde{z}_1 \in \Sigma_2^{NS} \cap \Sigma_2^{S}$). (e,f) Point $C2_4$: a 1-spiking periodic orbit grazes the threshold twice, both tangentially ($\tilde{z}_1 \in \Sigma_1^{S} \cap \Sigma_2^{S}$).

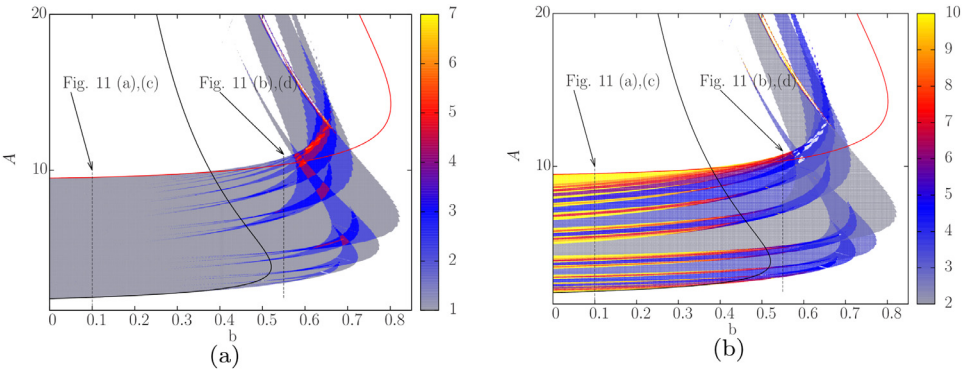

Fig. 10. (a) Number and (b) period of the periodic orbits of the stroboscopic map for $T = 0.5$ stepping on S_0 and S_1 found by means of the numerical algorithm described in Appendix D. We include also the bifurcation curves computed in Fig. 4. All periodic orbits are maximin. The areas where there is coexistence of two or more periodic orbits are colored according to an averaged period in order to reflect superposition of colors. Regions with orbits of period equal or higher than 10 have the same color. Notice that the region where periodic orbits exist shows a jagged edge due to numerical issues related to grazing of the orbits.

of a point of the orbit z_i with the border Σ_1 and Σ_2, bounding the region of existence of a given periodic orbit. Take for instance the orbit of period 2 $(z_1, z_2) \in (S_0 \cup S_1)^2$ (corresponding to the orbit with symbolic sequence 01, i.e $z_1 \in S_0$ and $z_2 \in S_1$, see Definition 1), which can be found in the region colored in gray (plus intersections) in Fig. 10(b). Notice that the shape of this region resembles that of the region of existence of $\bar{z}_1$ in Fig. 4 (recall that this region is bounded by the red curves). Clearly, the existence regions for different periodic orbits overlap as b increases giving rise to regions with multiple coexistence of periodic orbits.

For small values of b (close to 0), we observe that periodic orbits exist only in the region where the stroboscopic does not have fixed points and, moreover, these periodic orbits are unique. Thus, for a fixed small b, as the amplitude increases the fixed point $\bar{z}_0$ disappears through a border collision bifurcation with Σ_1^{NS} (black curve) and a unique periodic orbit appears, undergoing most likely a period-adding bifurcation (see also Fig. 11(a)) until the fixed point $\bar{z}_1$ appears through a border collision bifurcation with Σ_1^{NS} (see Section 6.2). The periodic orbits in this region are organized by bifurcation structures that resemble the period-adding bifurcation structure of 1-dimensional circle or discontinuous maps (see [19]). More precisely, their "rotation number" (see Definition 3 and Remark 8) resembles the devil's staircase, symbolic sequences of periodic orbits are glued through gluing bifurcations and their periods are added. See Fig. 11(a) and Fig. 11(c), where we show the periods and the "rotation number", respectively, of the periodic orbits along the 1-dimensional scan for $b = 0.1$ (labeled in Fig. 10(a)).

Remark 11. We emphasize that we refer to period-adding-like or cascade of gluing bifurcations when we cannot assess that we have the infinite number of bifurcation curves that separate the regions of existence of periodic orbits or, equivalently, a continuous curve of "rotation numbers", showing a devil's staircase through the complete Farey tree.

For intermediate and large values of b (approximately 0.5 and above) there exist multiple periodic orbits of the stroboscopic map that coexist with fixed points. Indeed, the regions of existence of periodic orbits expand towards the regions where $\bar{z}_0$ or $\bar{z}_1$ also exist, while at the same time start to intersect between them, showing multistability. Moreover, many branches of "rotation numbers" are lost, leaving the Farey tree incomplete. See for example a one-dimensional scan for $b = 0.55$ in Fig. 12(b), where many periodic orbits are no longer found and one finds co-existence instead. Consequently, the "rotation number" (shown in Fig. 11(d)) is discontinuous, leading to the coexistence of periodic orbits and overlapping of rotation numbers.

For $T = 5$ we observe that for all values of b between 0 and 1, periodic orbits only exist in the region confined between two nonsmooth border collision bifurcations, corresponding to the disappearance of the fixed point $\bar{z}_0$ ($\bar{z}_0$ impacts Σ_1^{NS}) and the appearance of the fixed point $\bar{z}_1$ ($\bar{z}_1$ impacts Σ_1^{NS}). See Fig. 12(a). In this case periodic orbits are all unique: we do not observe coexistence of several periodic orbits or coexistence of periodic orbits with fixed points. For a fixed value of b, as the amplitude A increases these periodic orbits undergo several gluing bifurcations (see also Fig. 12(b)). However, in this case our numerical computations suggest that the Farey tree is incomplete and the curve or "rotation numbers" shows discontinuities without the overlapping observed in the previous case.

Notice that, as opposed to the case $T = 0.5$, periodic orbits are confined in a very small region of the bifurcation diagram. Alongside, for the case $T = 0.5$ most of the border collision bifurcations correspond to collisions with Σ_1^{NS} and Σ_2^{NS}, i.e., nonsmooth grazing bifurcations. In this case, it is expected that close to a border collision the dynamics of the map will map points of S_0 to S_1 and viceversa, and therefore there might appear periodic orbits whose iterates step on both regions S_0 and S_1. However, for $T = 5$, for intermediate and large values of b border collision bifurcations correspond to collisions with Σ_1^S and Σ_2^S, and in this case we do not find periodic orbits stepping only on S_0 and S_1. Instead, it seems that fixed points $\bar{z}_0$ and $\bar{z}_1$ coexist, thus possibly preventing the existence of periodic orbits. The further exploration of the dynamics close to border collision bifurcations with Σ_1^S and Σ_2^S lies ahead (see Section 7 for a discussion).

6.4. Maximin itineraries

In this section we explore the maximin properties of the computed periodic orbits for the stroboscopic map (see equivalent Definitions 5 and 6). Using a simple algorithm (see Appendix D for details), we find that all the itineraries are maximin. In Fig. 13 we show the time series of the periodic orbits obtained for the parameter values labeled in Fig. 11(a) for $T = 0.5$. Their symbolic itineraries are 01^5, 0101^2, $001(01)^3$ and 0^71, which are all maximin. Recalling Definition 1, symbol 0 is used when no spike is produced ($z_i \in S_0$), while 1 means that one spike is produced ($z_i \in S_1$). To study the existence of maximin itineraries more rigorously we wonder if the conditions of Theorem 1 are satisfied. Notice though that conditions *i)–iii)* are difficult to check explicitly and therefore we designed an algorithm to check them numerically. Next, we describe the numerical algorithm and discuss the domain of application of the theoretical result.

For a given value of A, we first numerically find sets E_i that satisfy hypothesis *i)* of Theorem 1. We construct these sets to be as small as possible and later we check whether they satisfy conditions *ii)* and *iii)*. For convenience, we choose these sets to be quadrilaterals whose union is a convex polygon. More complex geometries are of course possible, although they would significantly complicate the algorithm without guarantee of better results.

To construct the sets E_0 and E_1, we first take a small segment $\gamma \subset \Sigma_1$ "close" to the periodic orbit found by direct simulation. This segment is iterated by $\mathfrak{s}_0$ and $\mathfrak{s}_1$. We then consider the two quadrilaterals formed by the segments γ and $\mathfrak{s}_0(\gamma)$, and γ and $\mathfrak{s}_1(\gamma)$ (see Fig. 14). We then grow the segment γ until the union of these two quadrilaterals is a convex polygon. If this cannot be done, then we stop the algorithm and assume we could not find the desired sets E_0 and E_1. If

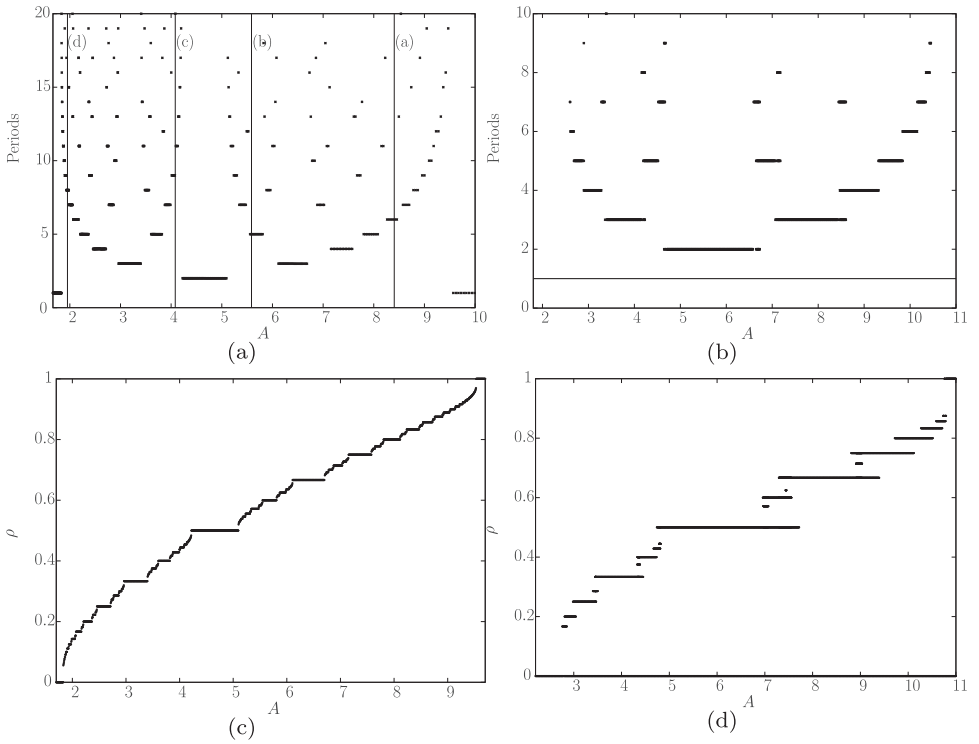

Fig. 11. Periods (top) and "rotation numbers" (bottom) of the periodic orbits found by varying the amplitude A along the vertical lines $b = 0.1$ (left) and $b = 0.55$ (right) as indicated in Fig. 4. Periodic orbits have been computed numerically using the algorithm described in Appendix D. For $b = 0.1$, we repeated the computations with a smaller stepsize along the A-axis and we have found higher periods interleaved according to the Farey tree structure (results not shown), suggesting that the "rotation number" shown in (c) might be continuous along the Farey tree.

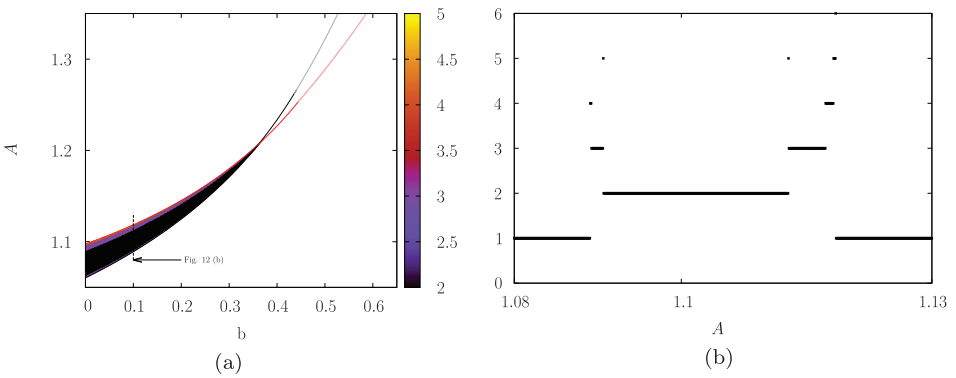

Fig. 12. (a) Periods of unique maximin periodic orbits of the stroboscopic map for $T = 5$ stepping on S_0 and S_1. We include also the bifurcation curves computed in Fig. 7. (b) Periods of the periodic orbits found by varying the amplitude A along the vertical line $b = 0.1$ as indicated in panel (a).

we succeed, we check whether the images of the two quadrilateral candidates are contained in their union (the convex polygon). The fact that their union is a convex polygon makes it easier to check this inclusion (see Remark 13). If any of the images is not contained in this union, then we further grow the initial segment γ in the direction that failed and we check again. If at some point we succeed, then we have found sets E_i satisfying hypothesis *i)* of Theorem 1. For the four values of A indicated in Fig. 11(a) we have been able to find sets E_0 and E_1 as described (see Fig. 14).

We then check the contracting condition *ii)*. As discussed in Section 3.2, , in general, the maps $\mathfrak{s}_i$ are contracting if d is small enough. In this particular example, provided that system (22) always possesses an attracting equilibrium point for $A \geq 0$ (although it may be virtual), the map $\mathfrak{s}_0$ is contracting for any $0 \leq d \leq 1$. This is because, in this case, $\mathfrak{s}_0$ becomes the composition of two stroboscopic maps of contracting flows. However, $\mathfrak{s}_1$ does not necessary contract, even if system (22) possesses for both $I = A$ and $I = 0$ attracting equilibrium points, due to the collision with the threshold and the reset condition. This is because, when spikes are introduced, the differential $D\mathfrak{s}_1$ is not only given by integration of variational equations, but it includes terms given by the reset map $\tilde{R}$ and differentiation of t_* with respect to initial conditions

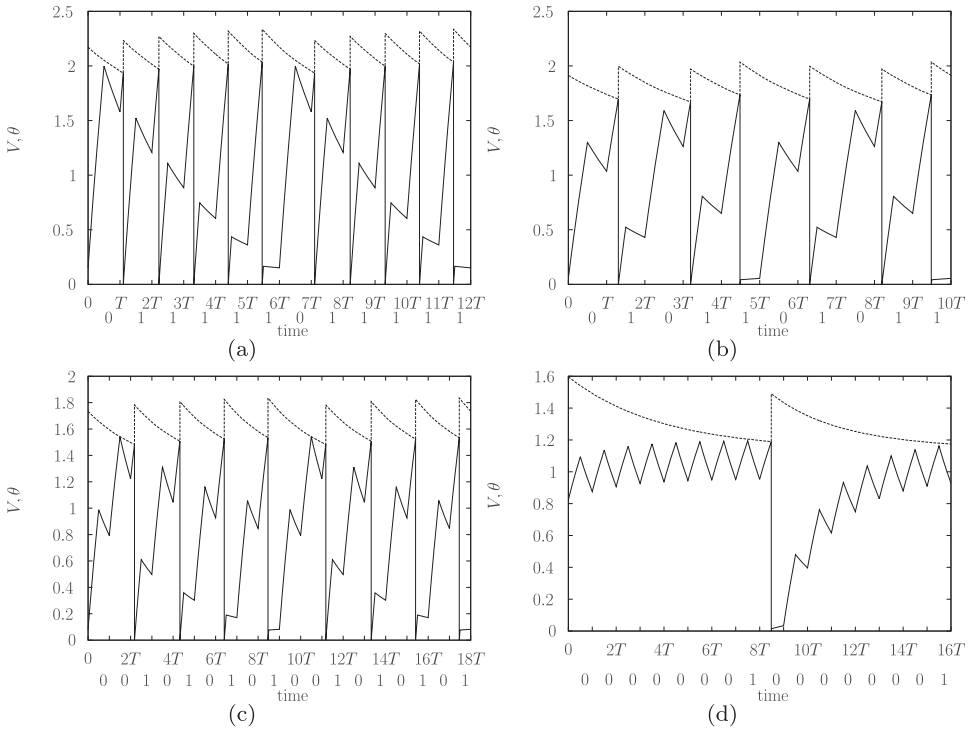

Fig. 13. Time course of the variables V (solid) and θ (dashed) corresponding to the four nT-periodic orbits labeled in Fig. 11(a) (with $n = 6$, 5, 9 and 8 for panels (a–d), respectively). Notice that we show two periods of the nT-periodic orbits. We indicate their symbolic itinerary at the bottom of the time axis.

(see Appendix B for more details). We check its contractiveness by numerically computing the differential $D\mathfrak{s}_1$ (as described in Appendix B) and its eigenvalues in a mesh of points in E_1. If, for all the points in the mesh, both eigenvalues have modulus less than 1 we then assume that condition *ii)* is also satisfied. If this condition is not fulfilled, we then say that we have not been able to check the conditions of Theorem 1. This is the case in panels (c) and (d) of Fig. 14, for which we have found points for which the matrix $D\mathfrak{s}_1$ has eigenvalues outside the unit circle.

Finally, it remains to check whether condition *iii)* holds. This is done by checking whether all points in the segment $\gamma \subset \Sigma_1$ visit S_0 and S_1 altogether or they split after intersecting $\Sigma_1(\mathfrak{s}^n(\gamma) \cap \Sigma_1$ for some $n > 0$). In other words, we numerically check whether all points in γ, are attracted towards the same fixed point of $\mathfrak{s}^p$, where p is the period of the periodic orbit found by iteration. In Fig. 14 we show examples of values of A for which condition *iii)* is satisfied (panels (a), (b) and (d)) and not satisfied (panel (c)). Thus, we conclude that for parameter values (A, b) corresponding to cases (a) and (b) we have checked semi-rigorously that the conditions of Theorem 1 are satisfied. Therefore, we get that a periodic orbit exists, its itinerary has to be maximin. We want to acknowledge that this numerical validation does not follow a computer assisted proof procedure.

We have applied the numerical algorithm described above to all values of A in Fig. 11(a). In Fig. 15 we show the values of A for which we have been able to validate conditions *i)–iii)* of Theorem 1.

Notice that hypothesis of Theorem 1 are difficult to check and very restrictive. Indeed, maximin periodic orbits exist far beyond the regions where the hypothesis can be checked using the numerical algorithm described above. Future work will be devoted to study the viability of the application of the techniques developed in [30] to cases with multistability.

Remark 12. This algorithm has more chances to suceed if the segment $\gamma \subset \Sigma_1^{\mathrm{NS}}$, which is the case in this example, as the computed periodic orbits are located between the curves defining $\bar{z}_0 \in \Sigma_1^{\mathrm{NS}}$ and $\bar{z}_1 \in \Sigma_1^{\mathrm{NS}}$.

Remark 13. This algorithm takes advantage of the fact that the sets E_i are quadrilaterals and that $E_0 \cup E_1$ is a convex polygon in order to easily check the inclusions $\mathfrak{s}_0(E_0) \subset E_0 \cup E_1$ and $\mathfrak{s}_1(E_1) \subset E_0 \cup E_1$. In order to check if a point lies in the interior of this polygon we order its vertices clockwise and check whether the vectors pointing from the point to these vertices twist clockwise. We do this for the iterates of a mesh of 50 points along the bondary of the polygon. If all images lie in the interior of $E_0 \cup E_1$, we then say the condition *ii)* is satisfied.

7. Conclusions and discussion

In this paper, we have studied the dynamics of hybrid systems submitted to a periodic forcing consisting of a square-wave pulse. In particular, we have studied a model consisting of a leaky integrate-and-fire model with a dynamic threshold,

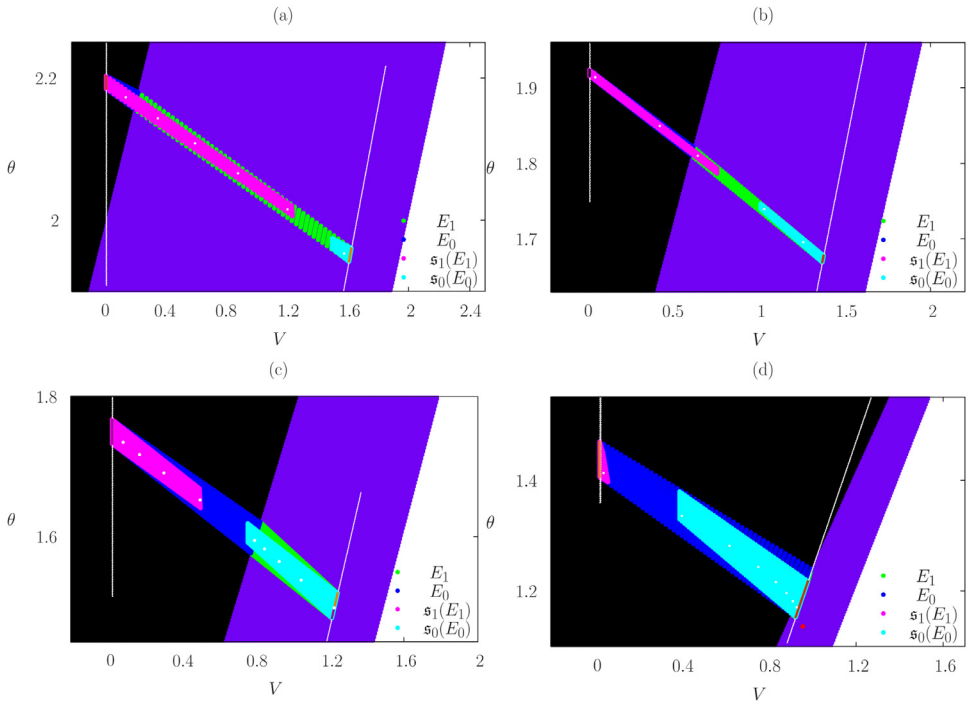

Fig. 14. Sets E_i satisfying condition *i) of Theorem 1 for the parameter values labeled in Fig. 11(a). The found periodic orbits have symbolic itineraries: (a)* 01^5, *(b)* 0101^2, *(c)* $0^21(01)^3$ *and (d)* 0^71. *The corresponding evolution of V and* θ *with respect to time is shown in Fig. 13. White points are the periodic orbit found by direct simulation. Red point is a virtual fixed point found by exteding the maps* $\mathfrak{s}_i$ *in their virtual domains, as explained in Section 3.2. Black background is* S_0, *blue background is* S_1. *Blue and green sets are* E_0 *and* E_1, *respectively. Pink and light blue are* $\mathfrak{s}_1(E_1)$ *and* $\mathfrak{s}_0(E_0)$, *respectively. The white lines are the images* $\mathfrak{s}_0(\Sigma_1)$ *and* $\mathfrak{s}_1(\Sigma_1)$. *Colored lines are the images of* γ *(see text) by* $\mathfrak{s}_i$. *Those segments that stay connected for all iterates of* $\mathfrak{s}$ *are plotted with the same color. For Figure (c), not all iterates of the* Σ_1 *stay connected and, hence, does not satisfy condition* iii). *For (c) and (d) we have found points in* E_1 *whose differential* $D\mathfrak{s}_1$ *has eigenvalues outside the unit circle, and hence condition* ii) is not satisfied. (a) and (b) satisfy conditions *i)–iii)* of Theorem 1. (For interpretation of the references to colour in this figure legend, the reader is referred to the web version of this article.)

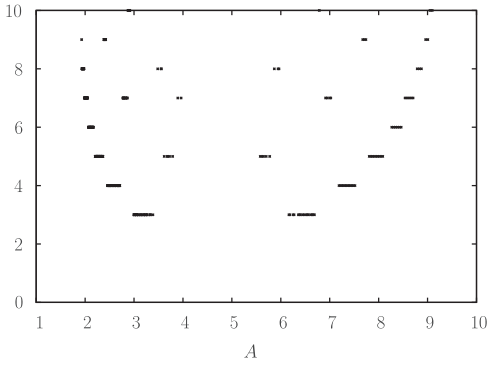

Fig. 15. Periods of the periodic orbits in Fig. 11(a) satisfying conditions of Theorem 1.

combined with a reset rule that is applied whenever the trajectory crosses the threshold manifold. In our analysis, we have considered the stroboscopic map, which is a piecewise-smooth discontinuous two-dimensional map, for which we can apply existing theoretical results by Gambaudo et al. [24,29] for "quasi-contractions" (see Theorem 1). Thus, we have been able to "prove", in combination with numerics, the existence of periodic orbits of maximin type for the stroboscopic map for certain parameter values. Moreover, we have explored numerically nonsmooth bifurcations (border collisions of fixed points and gluing bifurcations of T-periodic orbits), that provide a wider description of the dynamics.

Using particular geometries for the sets E_i (quadrilaterals with $E_0 \cup E_1$ being a convex polygon), we have shown that the existing theory has very restrictive hypothesis, since we have numerically observed the existence of maximin unique periodic orbits even for cases that do not satisfy the hypothesis of Theorem 1. Moreover, these hypothesis are difficult to check analytically. Indeed, we have designed a semi-rigorous numerical procedure to check them. It is possible that using more complex geometries and topologies for the sets E_i one could obtain better results in checking these hypothesis, although this

may signifficantly complicate the numerical algorithms. Thus, the existing theoretical results for two-dimensional piecewise continuous maps are still very limited to provide a complete description of the dynamics.

In our analysis we have considered only two partitions for the domain of the stroboscopic map, namely S_0 and S_1. We leave for future work the exploration of the invariant objects in other regions of the domain of the stroboscopic map, that is S_n for $n \geq 2$, as well as the exploration of other invariant objects beyond periodic orbits.

In our numerical analysis of nonsmooth bifurcations, we have varied the parameter b in Eq. (23) which sets the system in two different dynamical regimes. Thus, for small values of b (close to 0), in response to a constant input of sufficiently large amplitude, the system shows repetitive spiking (*tonic regime*). However, as b increases, a constant input cannot generate repetitive firing, only a few spikes before returning to resting potential (*phasic regime*) [6,7,31]. We have forced the system with a square-wave periodic pulse and explored fixed points and periodic solutions of the stroboscopic map in these two regimes as the amplitude A increases.

In the tonic regime, we have observed a unique globally attractive maximin periodic orbit with a period that, as the amplitude is increased, undergoes several gluing bifurcations mimicking the so-called period adding bifurcations for 1-dimensional maps. Thus, the transition from a T-periodic orbit with no spikes (fixed point $\bar{z}_0$) and a T-periodic orbit with a spike (fixed point $\bar{z}_1$) occurs through a complex mechanism of concatenation of sequences of periodic orbits whose "rotation number" is ordered as in the Farey tree. When we compare the results for two different input frequencies we observe different behaviours. For high frequency ($T = 0.5$), their "rotation number" evolves, up to our numerical accuracy, as in the 1-dimensional case; that is, it evolves continuously along the Farey tree showing a devil's staircase. This at least the case for periodic orbits with periods up to 30. In contrast to the high frequency case, for lower input frequency ($T = 5$), the "rotation number" becomes discontinuous. In other words, the Farey tree of "rotation numbers" is not complete. In both cases, the cascade of gluing bifurcations is confined in the region between two border collision bifurcations (where $\bar{z}_0$ and $\bar{z}_1$ do not exist).

The behavior drastically changes as b increases and the dynamical regime becomes phasic. The dynamics here is more complex and very different for $T = 5$ and $T = 0.5$. Thus, for $T = 0.5$ the organization of periodic orbits in a Farey tree gets destroyed by the overlap of neighboring periodic orbits (including periodic orbits of period 1 corresponding to $\bar{z}_0$ and $\bar{z}_1$), leading first to multistability and later to the disappearance of these periodic orbits of period higher than 1. In the case $T = 5$, periodic orbits of period higher than 1 (that step on S_0 and S_1) cannot be found beyond the regions where $\bar{z}_0$ and $\bar{z}_1$ do not exist. Notice that in this setting, for small values of A the system displays a T-periodic orbit with no spikes (fixed point $\bar{z}_0$) and as A increases there appears a T-periodic orbit with a spike (fixed point $\bar{z}_1$), and both T-periodic orbits coexist. This behavior agrees with the observation in [6] (for a periodic rectified sinusoidal input), where the transition from firing patterns consisting of a T-periodic orbit with no spikes to a T-periodic orbit with 1 spike, is more abrupt for low input frequencies. We leave for future work the exploration of the dynamics for other values of T.

Notice that b small sets the system in a dynamical regime (tonic) which can be modeled with a 1-dimensional integrate-and-fire system with a fixed threshold. However, as b increases the dynamical regime becomes phasic, and a one-dimensional integrate-and-fire model cannot reproduce these dynamics, thus suggesting that the results for larger values of b show characteristics of 2-dimensional systems. Alongside, conditions for the existence of a period-adding bifurcation (for which the rotation number is continuous and evolves showing a devil's staircase along the Farey tree) have been established theoretically for 1-dimensional piecewise maps [16]. However, it still remains an open question whether it can occur in 2-dimensional maps and under which conditions. We believe that our results might serve as a motivation and starting point to prove the conditions that guarantee the existence of period-adding structures in 2-dimensional hybrid systems. Indeed, as a future work, one might consider reducing the planar piecewise-smooth map to a map onto the cylinder and use rotation theory for these maps to provide explicit conditions for the existence of period adding bifurcations.

Regarding the implications for neural studies, our results provide a description of the dynamics and its parameter-dependence for a class of hybrid neuronal models with more realistic assumptions (variable thresholds). An important observation is that for certain parameter values, stable phase locked responses with different rotation numbers coexist. This is a novelty with respect to the classical 1-dimensional leaky integrate-and-fire model, where the rotation number is uniquely determined [14,16,17]. It remains an open question how the demonstrated properties for single neuron models translate to the dynamics of a network of neurons. For instance, one may wonder how the observed multistability in the phase-locked states would affect the network. In this case, a cell that is entrained to a network with a 1:1 phase-locking could be easily swicthed to another stable phase-locked state with a small peturbation, causing a change in the synchronization pattern. Hence, our work has possible relevance for the use of hybrid models with dynamic threshold to study impulse-based network desynchronization control techniques (see [32] and references therein), but further work lies ahead.

We recall that, in the nonsmooth literature, the concept of grazing bifurcation refers to a periodic orbit of a Filippov system that grazes a switching manifold (where the vector field has a discontinuity). As the vector field is smooth outside of the switching manifold, this grazing happens to be tangent. In some sense, this classical grazing bifurcation can be related to our case. After identifying the manifolds $\mathcal{T} \sim \mathcal{R}$ such that

$$\mathcal{T} \ni z_{\mathcal{T}} \sim z_{\mathcal{R}} \in \mathcal{R} \text{ if } z_{\mathcal{R}} = R(z_{\mathcal{T}}),$$

and adding time as a new variable one gets a Filippov system with three swtching manifolds ($\mathcal{T} \sim \mathcal{R}$, $\{t = dT \mod T\}$ and $\{t = 0 \mod T\}$). Then, what we called smooth grazing bifurcation corresponds to grazing the manifold $\mathcal{T} \sim \mathcal{R}$ only, while the nonsmooth grazing bifurcation corresponds to simultaneously grazing the manifold $\mathcal{T} \sim \mathcal{R}$ and crossing $\{t = dT \mod T\}$.

The first case becomes similar to the classical grazing with the addition of a second discontinuity surface which is not influencing the bifurcation [33]. In our work, however, we are not only interested in the conditions for which a T-periodic orbit bifurcates through grazing, but also on how are the dynamics after this bifurcation. We have shown that rich dynamics involving gluing bifurcations are generated when the grazing and crossing simultaneously occur.

Also regarding the nonsmooth literature, we emphasize that classical results [26,27,34–43] cannot be applied to our case mainly due to the periodic forcing, which makes the Poincaré map onto the grazed manifold 2-dimensional. Indeed, this is precisely the main reason why one finds so rich dynamics in this case. However, regarding multistability close to the grazing bifurcation, a similar phenomenon is also found for autonomous systems leading to 1-dimensional Poincaré maps [30,44] although one requires sliding motion along the switching manifold, which cannot be found in our case. We recall that, in this work we have focused on periodic orbits stepping on S_0 and S_1 only. A further analysis of the bifurcation structure close to the boundaries Σ_1^S and Σ_2^S may reveal that other type of periodic orbits also stepping on the sets S_i, $i>1$, may also appear and may be related with previous results on grazing bifurcations leading to multistability.

We finally point out that, also due to the periodic forcing, our analysis is different than others in the neuroscience literature [10–12,45]. Instead of considering the so-called firing or adaptation map (which is indeed the Poincaré map onto the switching manifold), our analysis is based on the stroboscopic map, which becomes a piecewise-smooth discontinuous map. The impact map has the advantage that is continuous but, as the system is non-autonomous, one would need to keep track of the time variable at the threshold manifold, which implies solving transcendental equations. Moreover, unlike the Poincaré map, the stroboscopic map is defined everywhere and hence captures subthreshold dynamics (dynamics not interacting with the threshold). Therefore, this latter map is the most suitable one to provide a complete description of the dynamics for the systems considered in this paper. Of course, the stroboscopic map is limited to periodic inputs. Indeed, if the stimulation of the neuron is not periodic, for instance, phase-modulated, the impact map would be more appropriate. For the case of an input consisting of an almost-periodic perturbation the firing rate dynamics was studied using the impact map in [46], although it provides limited information about the orbits.

Acknowledgments

This work has been partially supported by MINECO-Feder Spanish grants MTM2015-65715-P (AG and GH), MTM-2015-71509-C2-2-R (GH), the Catalan Grant 2017SGR1049 (GH), Marie Curie FP7 COFUND Ørsted fellowship (AG) and Ramón y Cajal fellowship 6-RYC-2014-15866. We also acknowledge the use of the UPC Dynamical Systems group's cluster for research computing (https://dynamicalsystems.upc.edu/en/computing/).

Appendix

This appendix contains the details of the numerical computations performed along the paper. In particular, we describe the computation of the switching manifolds for the stroboscopic map, its differential, the curves corresponding to border collision bifurcations of the fixed points of the stroboscopic map and the computation of the periodic orbits of the stroboscopic map.

Appendix A. Computation of the switching manifold

In this section we explain how to compute the switching manifolds Σ_n, and therefore the areas S_n in the subthreshold domain $\mathbb{D}$. In the case of Σ_n^{NS}, we take points on $\mathcal{T}$ and integrate them backwards in time for $t=dT$. If the trajectory hits the reset manifold $\mathcal{R}$, we apply R^{-1} (in the example considered, subtract Δ to the θ-variable and set $V=\theta$), count one hit and continue integrating the trajectory backwards for $t=dT$. If the trajectory hits $\mathcal{R}$ again for $t<dT$, we count another hit and we apply the same procedure as before. We keep the last point. It will belong to Σ_{n+1}^{NS}, where n counts the number of hits with the manifold $\mathcal{R}$. Of course, the trajectories always lie inside the subthreshold region. On the contrary, if one of these trajectories lies on the superthreshold region when integrating backwards, we may suspect that $\Sigma_n^S\neq\varnothing$. Then, we compute the point on the threshold manifold $\mathcal{T}$ where the trajectory is tangent. In the example considered, it must satisfy $V=\theta$ and $(-1,1)\cdot(f(V,\theta)+(A,0))=0$, or, equivalently, $(V-V_0-A)\tau_\theta-V+\theta_\infty(V)=0$. Once we find the point $(V,\ V)$ that solves the equations, we integrate this point backwards in time until $t=dT$. A point on this trajectory belongs to Σ_{n+1}^S, where n corresponds to the number of times the trajectory has hit the reset manifold before reaching the given point when integrated backwards.

Appendix B. The differential of the stroboscopic map

In this section we give details of the computation of the differential of the stroboscopic map $\mathfrak{s}$ in S_0 and S_1, that is, $D\mathfrak{s}_0$ and $D\mathfrak{s}_1$, for the general setting described in Section 2. The differential will be used to compute fixed points through a Newton method as well as their stability. Recall that $\mathfrak{s}_0$ is the composition of two stroboscopic maps (see Eq. (7)). Since $I(t)$ is a piecewise-constant function, the Jacobian matrix of the stroboscopic map can be computed by solving the variational

equations of system (1) for I constant. Calling $z = (x, y)$, these variational equations become

$$\frac{d}{dt}\delta_A(t;z) = \begin{pmatrix} \frac{\partial}{\partial x}f^x(\varphi_A(t;z)) & \frac{\partial}{\partial y}f^x(\varphi_A(t;z)) \\ \frac{\partial}{\partial x}f^y(\varphi_A(t;z)) & \frac{\partial}{\partial y}f^y(\varphi_A(t;z)) \end{pmatrix}\delta_A(t;z) \tag{B.1}$$

and

$$\delta_A(t;z) = \begin{pmatrix} \frac{\partial}{\partial x}\varphi_A^x(t;z) & \frac{\partial}{\partial y}\varphi_A^x(t;z)) \\ \frac{\partial}{\partial x}\varphi_A^y(t;z)) & \frac{\partial}{\partial y}\varphi_A^y(t;z)) \end{pmatrix},$$

where φ_A^x, φ_A^y, f^x and f^y denote the x and y component of the flow φ_A and the vector field f, respectively. Eq. (B.1) must be integrated along with the flow $\varphi_A(t; z)$ using the identity matrix as initial condition for δ_A, i.e $\delta_A(0; z) = Id$.

Hence, for $z \in S_0$, we have

$$D\mathfrak{s}_0(z) = \delta_0(T - dT; \varphi_A(dT; z)) \cdot \delta_A(dT; z). \tag{B.2}$$

In order to compute the differential $D\mathfrak{s}_1$ (see definition of $\mathfrak{s}_1$ in Eq. (12)), we need to take into account that the firing time, t_*, depends on the initial conditions, i.e. $t_* = t(z)$. Thus, we compute Dt by means of applying the Implicit Function Theorem to the equation

$$F(t, z) := h(\varphi_A(t; z)) = 0. \tag{B.3}$$

Let (t_*, z) be a solution of Eq. (B.3); that is, $\varphi_A(t_*; z) \in \mathcal{T}$. Then, assuming that

$$\frac{\partial F}{\partial t}(t_*, z) = \nabla h(\varphi_A(t_*; z))\frac{d\varphi_A}{dt}(t_*; z) \neq 0, \tag{B.4}$$

we obtain $t^* = t(z)$ and

$$Dt(z) = -\frac{\partial F/\partial z}{\partial F/\partial t} = -\frac{\nabla h(\varphi_A(t_*; z)) \cdot \delta_A(t_*; z)}{\nabla h(\varphi_A(t_*; z)) \cdot (f(z) + \nu A)}.$$

Note that condition (B.4) is equivalent to requiring that the flow is not tangent to $\mathcal{T}$ at $\varphi_A(t_*; z)$, and hence this is only valid when the spike is given by a transversal crossing between the flow and $\mathcal{T}$.

Then, the differentials of the maps (8)–(11) are

$$DP_1(z) = \begin{pmatrix} \delta_A(t_*; z) + (f(z) + \nu A)Dt(z) \\ Dt(z) \end{pmatrix}$$

$$D\tilde{R}(z, t) = \begin{pmatrix} DR(z) & \begin{matrix} 0 \\ 0 \end{matrix} \\ \begin{matrix} 0 & 0 \end{matrix} & 1 \end{pmatrix}$$

$$D\tilde{P}_2(z, t) = \begin{pmatrix} \delta_A(dT - t; z) & -(f(z) + \nu A) \end{pmatrix}$$

$$DP_3(z) = \delta_0(T - dT; z).$$

Hence, we get

$$D\mathfrak{s}_1(z) = DP_3(z_2)D\tilde{P}_2(z_r, t_1)D\tilde{R}(z_1, t_1)DP_1(z),$$

where

$$(z_1, t_1) = P_1(z) \quad (z_r, t_1) = \tilde{R}(z_1, t_1) \quad z_2 = \tilde{P}_2(z_r, t_1).$$

Remark 14. Notice that in the computation of DP_1 we take into account that the original and perturbed orbit do not cross the switching manifold at the same time. The method described herein to compute DP_1 is equivalent to the one developed in [47], later adopted by the nonsmooth and mechanical-engineering community and named *saltation* (or *correction*) matrix [48].

Appendix C. Numerical computation of bifurcation curves

The set of equations describing the bifurcation curves consist always of n equations and $n + 1$ unknowns, defining a curve on an n-dimensional space. In this section we will present a predictor-corrector method to compute such curves. The corrector step is based on a Newton method and Lagrange multipliers. We refer to [49] for further details. In https://github.com/a-granados/ContLagMult we provide the code of a general purpose implementation of this method in C^{++}. In this repository we also provide, to serve as example, the details to compute all bifurcation curves discussed in Section 6.2.

Let $\mathcal{G}(w) = 0$ be the set of n equations with $w \in \mathbb{R}^{n+1}$. Assume that there exists $w^* \in \mathbb{R}^{n+1}$ such that $\|\mathcal{G}(w^*)\|$ is small. We look for an improved solution by means of a Newton method. Thus, we look for Δw such that $w^* + \Delta w$ solves equation

$\mathcal{G}(w) = 0$ up to square order, i.e we impose that $\mathcal{G}(w^*) + D\mathcal{G}(w^*)\Delta w = 0$, with the extra condition that $\|\Delta w\|_2$ is a minimum. It becomes a poblem of finding the local minima subject to an equality constraint, which we will solve using the method of Lagrange multipliers. We introduce the Lagrange multiplier $\mu \in \mathbb{R}^n$ and the Lagrange function:

$$\mathcal{L} = \Delta w^T \Delta w + \mu^T (D\mathcal{G}(w^*)\Delta w + \mathcal{G}(w^*)).$$

Now imposing that $\partial\mathcal{L}/\partial(\Delta w) = 0$ and using the equality constraint, we are left with the following system of equations for μ and Δw:

$$\begin{array}{rcl} 2\Delta w^T + \mu^T D\mathcal{G}(w^*) & = & 0, \\ \mathcal{G}(w^*) + D\mathcal{G}(w^*)\Delta w & = & 0, \end{array}$$

from where we obtain $\Delta w = -D\mathcal{G}(w^*)^T (D\mathcal{G}(w^*)D\mathcal{G}(w^*)^T)\mathcal{G}(w^*)$. We repeat the process until we obtain a point w_{new} that satisfies equation $\mathcal{G}$ up to the desired error. This provides a point on the curve. The next step is to compute another point on the curve. To do so, we compute the tangent vector to the curve at the point w_{new} and take a point at a distance δ along this direction. Notice that the tangent vector is given by an element of the kernel of $D\mathcal{G}(w_{new})$. This will be the initial seed to repeat the Newton method procedure described above.

To illustrate the method, we provide the details for the computation of two of the bifurcation curves reported in Section 6.2, corresponding to $\bar{z}_1 \in \Sigma_1^{\mathrm{NS}}$ and $\bar{z}_1 \in \Sigma_1^{\mathrm{S}}$; the rest of the bifurcation curves can be obtained proceeding similarly.

For the case $\bar{z}_1 \in \Sigma_1^{\mathrm{NS}}$, the function $\mathcal{G}$ is given by Eqs. (29), and becomes

$$\mathcal{G}(\omega) = \begin{pmatrix} \varphi_A(-t_1; V_1, V_1) - \varphi_0(T - dT; V_2, V_2) \\ (V_2, V_2)^T - \varphi_A(dT - t_1; V_r, V_1 + \Delta) \end{pmatrix},$$

with $\omega = (V_1, V_2, t_1, b, A) \in \mathbb{R}^5$. Note that $\mathcal{G}(w) \in \mathbb{R}^4$, as the flow is 2-dimensional. The derivatives in $D\mathcal{G}$ involving the variables V_1, V_2 are obtained integrating the variational equations of system (22), and the ones involving t_1 are given by the vector field. Regarding the derivatives with respect to parameters b and A, one needs to consider them as variables of the system and increase its dimension from 2 to 4 by adding the equations $\dot{b} = 0$ and $\dot{A} = 0$. Then, the derivatives with respect to b and A are obtained from the variational equations of this new extended system. Using the notation of Appendix B, the variational equations for the extended system become

$$\frac{d}{dt}\tilde{\delta}_A = \begin{pmatrix} Df(\varphi_A(t;z)) & & 0 & \frac{\partial}{\partial A} f^V(\varphi_A(t;z)) \\ & & \frac{\partial}{\partial b} f^\theta(\varphi_A(t;z)) & 0 \\ 0 & 0 & 0 & 0 \\ 0 & 0 & 0 & 0 \end{pmatrix} \tilde{\delta}_A \tag{C.1}$$

where

$$\tilde{\delta}_A(t; z, b, A) = \begin{pmatrix} \delta_A(t;z) & & \frac{\partial}{\partial b}\varphi_A^V(t;z) & \frac{\partial}{\partial A}\varphi_A^V(t;z) \\ & & \frac{\partial}{\partial b}\varphi_A^\theta(t;z) & \frac{\partial}{\partial A}\varphi_A^\theta(t;z) \\ 0 & 0 & 1 & 0 \\ 0 & 0 & 0 & 1 \end{pmatrix},$$

and $\delta_A(t; z)$ is defined in Appendix B with $z = (V, \theta)$.

With this notation we get

$$\frac{\partial}{\partial V_1}\mathcal{G}(V_1, V_2, t_1, b, A) = \begin{pmatrix} \delta_A^{1,1}(-t_1; V_1, V_1) + \delta_A^{1,2}(-t_1; V_1, V_1) \\ \delta_A^{2,1}(-t_1; V_1, V_1) + \delta_A^{2,2}(-t_1; V_1, V_1) \\ -\delta_A^{1,2}(dT - t_1; V_r, V_1 + \Delta) \\ -\delta_A^{2,2}(dT - t_1; V_r, V_1 + \Delta) \end{pmatrix},$$

$$\frac{\partial}{\partial V_2}\mathcal{G}(V_1, V_2, t_1, b, A) = \begin{pmatrix} -\delta_0^{1,1}(T - dT; V_2, V_2) - \delta_0^{1,2}(T - dT; V_2, V_2) \\ -\delta_0^{2,1}(T - dT; V_2, V_2) - \delta_0^{2,2}(T - dT; V_2, V_2) \\ 1 \\ 1 \end{pmatrix}$$

$$\frac{\partial}{\partial t_1}\mathcal{G}(V_1, V_2, t_1, b, A) = \begin{pmatrix} -(f^V(z_1) + A) \\ -f^\theta(z_1) \\ f^V(z_2) + A \\ f^\theta(z_2) \end{pmatrix} \begin{array}{l} z_1 = \varphi_A(-t_1; V_1, V_1) \\ z_2 = \varphi_A(dT - t_1; V_r, V_1 + \Delta), \end{array}$$

$$\frac{\partial}{\partial b}\mathcal{G}(V_1,V_2,t_1,b,A)=\begin{pmatrix}\tilde{\delta}_A^{1,3}(-t_1;V_1,V_1,b,A)-\tilde{\delta}_0^{1,3}(T-dT;V_2,V_2,b,A)\\ \tilde{\delta}_A^{2,3}(-t_1;V_1,V_1,b,A)-\tilde{\delta}_0^{2,3}(T-dT;V_2,V_2,b,A)\\ -\tilde{\delta}_A^{1,3}(dT-t_1;V_r,V_1+\Delta,b,A)\\ -\tilde{\delta}_A^{2,3}(dT-t_1;V_r,V_1+\Delta,b,A)\end{pmatrix},$$

and

$$\frac{\partial}{\partial A}\mathcal{G}(V_1,V_2,t_1,b,A)=\begin{pmatrix}\tilde{\delta}_A^{1,4}(-t_1;V_1,V_1,b,A)\\ \tilde{\delta}_A^{2,4}(-t_1;V_1,V_1,b,A)\\ -\tilde{\delta}_A^{1,4}(dT-t_1;V_r,V_1+\Delta,b,A)\\ -\tilde{\delta}_A^{2,4}(dT-t_1;V_r,V_1+\Delta,b,A)\end{pmatrix}.$$

Similarly, for the smooth grazing bifurcation corresponding to $\tilde{z}_1\in\Sigma_2^S$ the function $\mathcal{G}$ is given by Eqs. (30) and has the form

$$\mathcal{G}(\omega)=\begin{pmatrix}\varphi_A(-t_1;(V_1,V_1))-\varphi_0(T-dT;\varphi_A(dT-t_1-t_2;V_2,V_2))\\ (V_2,V_2)^T-\varphi_A(t_2;V_r,V_1+\Delta)\\ -V_2+V_0+A-1/\tau_\theta(-V_2+\theta_\infty(V_2))\end{pmatrix},$$

with $\omega=(V_1,V_2,t_1,t_2,b,A)\in\mathbb{R}^6$. Note that now $\mathcal{G}\in\mathbb{R}^5$, and the last equation imposes a tangency when reaching the threshold at $(V_2,\ V_2)$. The differential $D\mathcal{G}$ is obtained proceeding as before taking into account that we need to apply the chain rule due to the composition $\varphi_0\circ\varphi_A$.

Appendix D. Numerical computation of periodic orbits

In this section we describe the algorithm to compute periodic orbits of the stroboscopic map. In https://github.com/ghuguet/PerOrbVtheta we provide the code in C^{++} used to compute the periodic orbits for the stroboscopic map of system (22)–(24), considered in this paper.

Periodic orbits of the system are computed by integrating forward a set of initial conditions on the region S_0. For each initial condition we compute $N=100$ iterates of the stroboscopic map and we keep the last point x_f in a list of points L_f as well as the previous one x_a ($x_f=\mathfrak{s}(x_a)$) in a list of points L_a. We also keep track of the number of spikes that occur between x_a and x_f. When several initial conditions yield the same points x_a and x_f, we keep them only once. Once we have computed the iterations for all points in the subthreshold domain, we check whether the points in the list L_a coincides with the points in the list L_f. If there is a point $\bar{x}_a$ in L_a which is not present in L_f, we add $\bar{x}_a$ in the list L_f and $\mathfrak{s}^{-1}(\bar{x}_a)$ in the list L_a. Analogously, if a point $\bar{x}_f$ in L_f is not present in L_a, we add $\bar{x}_f$ in the list L_a and $\mathfrak{s}(\bar{x}_f)$ in the list L_f. We repeat this procedure until both lists contain the same points. If after several iterations both lists are still different, the program returns the message that the computation of periodic orbits has failed. Otherwise, once both lists are equal, we order them while constructing a map ν that maps the position i of the point x_a in the ordered list L_a to the position j of its image $x_f=\mathfrak{s}(x_a)$ in the ordered list L_f, i.e. $\nu(i)=j$. For each pair $(i,\ j)$ we also keep track of the number of spikes that occur. Let us call this number s_i A fixed point of the stroboscopic map corresponds to $\nu(i)=i$, while a periodic orbit of period q corresponds to

$$\nu^q(i)=i,\ \text{where}\ \nu^k(i)\neq i,\ \text{for}\ k=1,\dots,q-1.$$

Hence, we use the map ν to compute the number of fixed points and periodic orbits. Moreover, for each periodic orbit we compute its period q and for periodic orbits stepping only on S_0 and S_1, we keep its itinerary given by $(s_i,s_{\nu(i)},\dots,s_{\nu^{q-1}(i)})\in\{0,1\}^q$.

Using this itinerary we compute whether the periodic orbit is maximin. From a computational point of view, Definition 5 is not practical to decide whether a symbolic sequence is maximin or not. Instead, we use the following equivalent definition of maximin using the notion of $p,\ q$-ordered sequences (see [19] for details):

Definition 6. Let $\mathbf{x}\in W_{p,\ q}$ be a periodic symbolic sequence. Consider the (lexicographically) ordered sequence given by the iterates of $\mathbf{x}$ by σ

$$\sigma^{i_0}(\mathbf{x})<\sigma^{i_1}(\mathbf{x})<\sigma^{i_2}(\mathbf{x})<\ldots<\sigma^{i_{q-1}}(\mathbf{x}). \tag{D.1}$$

We say that the sequence $\mathbf{x}$ is a $p,\ q$-ordered (symbolic) sequence if

$$i_j-i_{j-1}=\text{constant}.$$

In other words, a sequence $\mathbf{x}\in W_{p,\ q}$ is $p,\ q$-ordered if σ acts on the sequence (D.1) as a cyclic permutation, i.e. there exists some $k\in\mathbb{N},\ 0<k<q$, such that

$$i_j=i_{j-1}+k\ (\text{mod}\ q). \tag{D.2}$$

Then, from [50], one has that a symbolic sequence $\mathbf{x}\in W_{p,\ q}$ is maximin if, and only if, it is $p,\ q$-ordered.

Using this definition, checking computationally whether a symbolic sequence is maximin becomes simpler and faster, as one does not need to compare, element by element, the sequence with the rest of sequences in the set $W_{p,\ q}$. The algorithm is as follows. Given a symbolic sequence $\mathbf{x}\in W_{p,\ q}$ we consider the q sequences given by $\sigma^i(\mathbf{x})$ with $0\leq i<q$. To

order them lexicographically, we simply consider them as integer numbers written in binary. Thus, for a symbolic sequence $\mathbf{x} = (x_0, \ldots, x_{q-1})$ we compute

$$a(\mathbf{x}) = \sum_{i=0}^{q-1} x_i 2^i.$$

Let us define $a_i := a(\sigma^i(\mathbf{x}))$. Then, note that $\sigma^i(\mathbf{x}) < \sigma^j(\mathbf{x})$ if, and only if, $a_i < a_j$. Hence we easily get a sequence

$$a_{i_0} < a_{i_1} < \cdots < a_{i_{q-1}}.$$

Then, if condition (D.2) is satisfied for all indices i_j, $0 \le j < q$ the sequence $\mathbf{x}$ is maximin.

References

[1] Izhikevich E. Dynamical systems in neuroscience: the geometry of excitability and bursting. Computational Neuroscience. Cambridge, MA: MIT Press; 2007.
[2] Izhikevich E. Simple model of spiking neurons. IEEE Trans Neural Networks 2003;14(6):1569–72.
[3] Brette R, Gerstner W. Adaptive exponential integrate-and-fire model as an effective description of neuronal activity. J Neurophysiol 2005;94:3637–42.
[4] Platkiewicz J, Brette R. A threshold equation for action potential initiation. PLoS Comput Biol 2010;6(7):e1000850.
[5] Higgs M, Spain W. Kv1 channels control spike threshold dynamics and spike timing in cortical pyramidal neurones. J Physiol (Lond) 2011;589:5125–42.
[6] Meng X, Huguet G, Rinzel J. Type III excitability, slope sensitivity and coincidence detection. Disc Cont Dyn Syst 2012;32:2720–57.
[7] Huguet G, Meng X, Rinzel J. Phasic firing and coincidence detection by subthreshold negative feedback: divisive or subtractive or, better, both. Front Comput Neurosci 2017;11:3.
[8] Makarenkov O, Lamb J. Dynamics and bifurcations of nonsmooth systems: a survey.. Physica D 2012;241:1826–44.
[9] Bernardo Md, Budd CJ, Champneys AR, Kowalczyk P. Piecewise-smooth dynamical systems: theory and applications. Applied Mathematical Sciences, 26. Springer; 2008.
[10] Touboul J, Brette R. Spiking dynamics of bidimensional integrate-and-fire neurons. SIAM J Appl Dyn Syst 2009;8(4):1462–506.
[11] Rubin J, Signerska-Rynkowska J, Touboul J, Vidal A. Wild oscillations in a nonlinear neuron model with resets: (II) mixed-mode oscillations. Discrete Contin Dyn Syst Ser B 2017;22(10):4003–39.
[12] Rubin J, Signerska-Rynkowska, Touboul J, Vidal A. Wild oscillations in a nonlinear neuron model with resets: (i) bursting, spike-adding and chaos. Discrete Contin Dyn Syst Ser B 2017;22(10):3967–4002.
[13] Coombes S, Thul R, Wedgwood K. Nonsmooth dynamics in spiking neuron models. Physica D 2012;241(22):2042–57. Dynamics and Bifurcations of Nonsmooth Systems
[14] Keener J, Hoppensteadt F, Rinzel J. Integrate-and-fire models of nerve membrane response to oscillatory input. SIAM J Appl Dyn Syst (SIADS) 1981;41:503–17.
[15] Tiesinga P, Fellous JM, Sejnowski T. Spike-time reliability of periodically driven integrate-and-fire neurons. Neurocomputing 2002;44:195–200.
[16] Granados A, Krupa M, Clément F. Border collision bifurcations of stroboscopic maps in periodically driven spiking models. SIAM J Appl Dyn Syst 2014;13(4):1387–416.
[17] Granados A, Krupa M. Firing-rate, symbolic dynamics and frequency dependence in periodically driven spiking models: a piecewise-smooth approach. Nonlinearity 2015;28:1163–92.
[18] Geller W, Misiurevicz M. Farey–lorenz permutations for interval maps. Int J Bifurcation Chaos 2018;28:1–10.
[19] Granados A, Alsedà L, Krupa M. The period adding and incrementing bifurcations: from rotation theory to applications. SIAM Rev 2017;56(2):225–92.
[20] Ermentrout B, Terman D. Mathematical foundations of neuroscience.. New York: Springer; 2010.
[21] Alsedà L, Llibre J, Misiurevicz M. Combinatorial dynamics and entropy in dimension one. World Scientific; 2000.
[22] Gambaudo JM, Tresser C. Dynamique régulière ou chaotique. applications du cercle ou de l'intervalle ayant une discontinuité.. C R Acad Sc Paris, série I 1985;300:311–13.
[23] Gambaudo JM, Glendinning P, Tresser C. Collage de cycles et suites de farey. C R Acad Sc Paris, série I 1984;299:711–14.
[24] Gambaudo JM, Glendinning P, Tresser C. The gluing bifurcation: symbolic dynamics of the closed curves. Nonlinearity 1988;1:203–14.
[25] Bogoliubov N, Mitropolski Y. Asymptotic methods in the theory of non-linear oscillations. Gordon and Breach; 1961.
[26] Nordmark AB. Universal limit mapping in grazing bifurcations. Phys Rev E 1997;55(1):266–70.
[27] Bernardo Md, Budd CJ, Champneys AR. Normal form maps for grazing bifurcations in n-dimensional piecewise-smooth dynamical systems. Physica D 2001;160(3–4):222–54.
[28] Nusse HE, Ott E, Yorke JA. Border-collision bifurcations: an explanation for observed bifurcation phenomena. Phys Rev E 1994;49:1073–6.
[29] Gambaudo JM, Tresser C. On the dynamics of quasi-contractions. BOL SOC BRAS MAT 1988;19:61–114.
[30] Glendinning P, Kowalczyk P, Nordmark A. Attractors near grazing-sliding bifurcations. Nonlinearity 2012;25:1867–85.
[31] Rinzel J, Huguet G. Nonlinear dynamics of neuronal excitability, oscillations, and coincidence detection. Commun Pure Appl Math 2013;66(9):1464–94.
[32] Wilson D, Moehlis J. Clustered desynchronization from high-frequency deep brain stimulation. PLoS Comput Biol 2016;11(12):1–26.
[33] Donde V, Hiskens I. Grazing bifurcations in periodic hybrid systems. Proceedings of the 2004 International Symposium on Circuits and Systems 2004;4:697–700.
[34] Dankowicz H, Nordmark AB. On the origin and bifurcations of stick-slip oscillations. Physica D 2000;136(3–4):280–302.
[35] Dankowicz H, Zhao X. Local analysis of co-dimension-one and co-dimension-two grazing bifurcations in impact microactuators. Physica D 2005;202:238–57.
[36] Nordmark AB. Existence of periodic orbits in grazing bifurcations of impacting mechanical oscillators. Nonlinearity 2001;14(6):1517.
[37] Nordmark A, Kowalczyk P. A codimension-two scenario of sliding solutions in grazing-sliding bifurcations. Nonlinearity 2006;19:1–26.
[38] Simpson D. Sequences of periodic solutions and infinitely many coexisting attractors in the border-collision normal form. Int J Bifurcation and Chaos 2014;24:1–23.
[39] Simpson D. The structure of mode-locking regions of piecewise-linear continuous maps: i. nearby mode-locking regions and shrinking points. Nonlinearity 2017;30:382–444.
[40] Simpson D. The structure of mode-locking regions of piecewise-linear continuous maps: ii. skew sawtooth maps. Nonlinearity 2018;31:1905–39.
[41] Zhao X, Dankowicz H. Unfolding degenerate grazing dynamics in impact actuators. Nonlinearity 2006;19:399–418.
[42] Thota P, Dankowicz H. Continuous and discontinuous grazing bifurcations in impacting oscillators. Physica D 2006;214:187–97.
[43] Kowalczyk P. Robust chaos and border-collision bifurcations in non-invertible piecewise-linear maps. Nonlinearity 2005;18(2):485.
[44] Glendinning P., Kowalczyk P., Nordmark A.. Multiple attractors in grazing-sliding bifurcations in filippov-type flows. IMA J Appl Math2016.
[45] Jimenez N, Mihalas S, Brown R, Niebur E, Rubin J. Locally contractive dynamics in generalized integrate-and-fire neurons. SIAM J Appl Dyn Syst (SIADS) 2013;12:1474–514.
[46] Kasprzak P, Nawrocki A, Signerska-Rynkowska J. Integrate-and-fire models with an almost periodic input function. J Diff Eqs 2017;264(4):2495–537.
[47] Aizerman M, Gantmakher F. On the stability of periodic motions. J Appl Math Mech 1958;22(6):1065–78.

[48] Leine R, Nijmeijer H. Dynamics and bifurcations of non-smooth mechanical systems. Lecture Notes in Applied and Computations Mechanics, 18. Springer; 2004.
[49] Allgower E, Georg K. Introduction to numerical continuation methods, 45 of classics in applied mathematics. SIAM; 2003.
[50] Gambaudo JM, Lanford O III, Tresser C. Dynamique symbolique des rotations. C R Acad Sc Paris, série I 1984;299:823–6.